




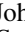






An Atmospheric Retrieval of the Brown Dwarf Gliese 229B

Emily Calamari^{1,2} , Jacqueline K. Faherty² , Ben Burningham³ , Eileen Gonzales^{4,8} , Daniella Bardalez-Gagliuffi⁵ ,
Johanna M. Vos² , Marina Gemma^{6,7} , Niall Whiteford² , and Josefine Gaarn³

¹ The Graduate Center, City University of New York, New York, NY 10016, USA; ecalamari@gradcenter.cuny.edu

² Department of Astrophysics, American Museum of Natural History, New York, NY 10024, USA

³ Centre for Astrophysics Research, School of Physics, Astronomy and Mathematics, University of Hertfordshire, Hatfield AL10 9AB, UK

⁴ Department of Astronomy and Carl Sagan Institute, Cornell University, 122 Sciences Drive, Ithaca, NY 14853, USA

⁵ Department of Physics & Astronomy, Amherst College, 25 East Drive, Amherst, MA 01003, USA

⁶ Department of Earth and Environmental Sciences, Columbia University, New York, NY 10027, USA

⁷ Department of Earth and Planetary Sciences, American Museum of Natural History, New York, NY 10024, USA

Received 2022 July 14; revised 2022 September 13; accepted 2022 September 28; published 2022 December 1

Abstract

We present results from an atmospheric retrieval analysis of Gl 229B using the Brewster retrieval code. We find the best fit model to be cloud-free, consistent with the T dwarf retrieval work of Line et al.; Zalesky et al. and Gonzales et al. Fundamental parameters (mass, radius, $\log(L_{\text{Bol}}/L_{\text{Sun}})$, $\log(g)$) determined from our model agree within 1σ to SED-derived values, except for T_{eff} where our retrieved T_{eff} is approximately 100 K cooler than the evolutionary model-based SED value. We find a retrieved mass of $50^{+12}_{-9} M_{\text{Jup}}$, however, we also find that the observables of Gl 229B can be explained by a cloud-free model with a prior on mass at the dynamical value, $70 M_{\text{Jup}}$. We are able to constrain abundances for H_2O , CO, CH_4 , NH_3 , Na and K and find a supersolar C/O ratio as compared to its primary, Gl 229A. We report an overall subsolar metallicity due to atmospheric oxygen depletion, but find a solar [C/H], which matches that of the primary. We find that this work contributes to a growing trend in retrieval-based studies, particularly for brown dwarfs, toward supersolar C/O ratios and discuss the implications of this result on formation mechanisms and internal physical processes, as well as model biases.

Unified Astronomy Thesaurus concepts: [Brown dwarfs \(185\)](#); [Atmospheric composition \(2120\)](#); [Companion stars \(291\)](#); [Fundamental parameters of stars \(555\)](#); [T dwarfs \(1679\)](#); [M dwarf stars \(982\)](#)

Supporting material: data behind figures

1. Introduction

With masses $\leq 75 M_{\text{Jup}}$, brown dwarfs are a category of astronomical objects whose core temperatures are too low to maintain stable hydrogen fusion throughout their lifetimes (Chabrier & Baraffe 1997). Unlike main sequence stars, brown dwarfs will contract and cool as they age and progress through their spectral classification sequence (M, L, T, Y; Kirkpatrick 2005; Burgasser et al. 2006; Cushing et al. 2011). These objects are often seen as a bridge between stars and planets, as they are luminous enough to be directly imaged, yet cool enough to have molecular-rich, and even condensate-rich, atmospheres, similar to what we see in Jupiter and large, gaseous exoplanets (e.g., Marley 1997; Marley et al. 2002, 2013; Helling & Casewell 2014). One path forward to understanding the breadth of exoplanet atmospheres, and the physical processes within them, is by proxy through brown dwarfs.

While important work has been done to characterize isolated brown dwarfs through computational approaches (e.g., Line et al. 2017; Burningham et al. 2021; Zalesky et al. 2022), in this work, we add to the list of retrieved companion objects by focusing on Gl 229B, the first discovered methane-bearing brown dwarf (Oppenheimer et al. 1995; Nakajima et al. 1995)

and a widely separated companion to a main sequence M-dwarf star, Gl 229A. Brown dwarfs that exist in co-moving pairs or systems, particularly ones with main sequence stars, have become critical benchmarks in order to further establish our understanding of substellar mass objects. Discoveries of these types of systems are essential to brown dwarf science, since we can use information from the primary star to place constraints on fundamental parameters for the system as a whole (e.g., Kirkpatrick et al. 2001; Burningham et al. 2009, 2011, 2013; Dupuy et al. 2009; Faherty et al. 2010, 2020, 2021; Pinfield et al. 2012). Such works have used chemical abundances, activity and/or kinematics of the primary star to place metallicity, mass and age constraints on the companion. However, inherent to these constraints is the assumption that these companion objects formed together via the same formation mechanism, which can bias our models and results.

Brown dwarf atmospheric research was initially grounded in the use of grid models (radiative-convective equilibrium atmosphere models) whose predicted spectra are fitted to observed spectra in order to derive fundamental properties of a particular object such as temperature, gravity and metallicity (e.g., Burrows et al. 1993; Burgasser et al. 2007). However, due to the complexity of these grid models, as well as the complexity and diversity of brown dwarf atmospheres, this method has been shown to produce discrepancies in parameter estimation and fitted synthetic spectra (e.g., Cushing et al. 2008; Rice et al. 2010; Manjavacas et al. 2014). In an attempt to constrain the previously estimated fundamental parameters of Gl 229B, we turn to atmospheric retrievals, a spectral inversion technique that compliments the work of forward grid

⁸ 51 Pegasi b Postdoctoral Fellow.



models by using minimal physical assumptions to determine more precise parameter values than are inferred by comparing synthetic to observed spectra.

For this retrieval work, we use Brewster, a flexible framework composed of a forward model and a retrieval model. The forward model reproduces the object spectrum based on a combination of pre-determined and retrieved parameters, while the retrieval model tests the goodness of fit of those parameters determined from the forward modeling and effectively proposes new parameter values (Burningham et al. 2017). This technique allows us to place constraints on gas abundances, thermal profile and, in the case of cloud models, cloud location and opacity.

In Section 2, we review published values of the Gl 229 system. In Section 3, we discuss the data used in constructing a spectral energy distribution (SED) as well as subsequent retrieval models and review SED-derived fundamental parameters for Gl 229B. In Section 4, we discuss the retrieval framework and settings used in our work. In Section 5, we present retrieval results for Gl 229B. In Section 6, we compare fundamental parameters derived from our retrieval model to literature predictions and SED-derived parameters. In Section 7, we place our work in the context of previous retrieval work on T dwarfs. Finally, in Section 8 we discuss retrieved C/O ratio and metallicity of Gl 229B and compare its retrieved chemistry to that of its primary, Gl 229A.

2. Literature Data on Gliese 229 System

2.1. Discovery, Observations and Mass Controversy of Gl 229B

The methane-bearing object that confirmed the existence of brown dwarfs in 1995 has been the subject of intense study and debate since its discovery. Separated from its primary at a distance of $7''.78 \pm 0''.1$, Gl 229B was initially found as a proper motion companion to an M1V star, Gl 229A (Oppenheimer et al. 1995; Nakajima et al. 1995). Initial observations of Gl 229B were done by Oppenheimer et al. (1995) who obtained a low-resolution near-infrared spectrum (1.0–2.5 μm) on the Hale 200 inch telescope, later followed up by higher resolution spectroscopic observations that would cover 0.8–5.0 μm (Geballe et al. 1996; Schultz et al. 1998; Saumon et al. 2000). These spectroscopic studies confirmed the presence of H₂O and CH₄ as well as CO in excess of the abundance predicted by chemical equilibrium. Broadband photometric observations obtained by Matthews et al. (1996), Golimowski et al. (1998), Leggett et al. (1999), Golimowski et al. (2004), combined with a Hipparcos parallax for Gl 229A (Perryman et al. 1997), since updated in Gaia Collaboration et al. (2021), resulted in a robust determination of its bolometric luminosity.

Several works have attempted to reproduce Gl 229B's spectra using thermo-chemical equilibrium models and subsequently derive its fundamental parameters to varied results. One initial spectroscopic study used PHOENIX grid models (Allard et al. 1996) to place upper limits on the effective temperature at 1000 K in an attempt to constrain the mass. However, uncertainties in the age of this system cause a significant challenge in determining fundamental parameters, such as mass, across several forward modeling attempts. As spectroscopic and photometric observations improved, Saumon et al. (2000) employed evolutionary models of Burrows et al. (1997) but

were still not able to constrain $\log(g)$ better than 5.0 ± 0.5 , although they predicted an atmosphere depleted in heavy metals, particularly oxygen. More recent work by Nakajima et al. (2015) attempted to use measured abundances and an age estimate of Gl 229A to determine an approximately solar metallicity for Gl 229B, assuming coevolution of the pair. Filippazzo et al. (2015) derives fundamental parameters based on the evolutionary models of Baraffe et al. (2003) and Saumon & Marley (2008) to create a distance-calibrated SED and directly integrated bolometric luminosity (L_{Bol}). A summary of fundamental parameters for Gl 229B can be found in Table 6.

While uncertainty in age estimates for the system posed a challenge in spectroscopic modeling carried out shortly after its discovery, a dynamical mass measurement for Gl 229B highlights this tension even further. Brandt et al. (2021) used astrometry from Gaia Collaboration et al. (2021) to constrain a dynamical mass at $71.4 \pm 0.6 M_{\text{Jup}}$, placing Gl 229B at the edge of the stellar mass boundary. All evolutionary model predictions prior to this work estimate an upper limit on age to be <5 Gyr based on its bolometric luminosity and derived effective temperature, with one work even suggesting Gl 229B is as young as 16 Myr (Leggett et al. 2002a). A predicted mass as high as that reported in Brandt et al. (2020, 2021) acutely challenges this age estimate, since an object this massive would take much longer to cool to its reported luminosity and approximate temperature of 900 K. In fact, Gl 229B is on a growing list of T dwarfs whose high masses conflict with what one might expect from evolutionary models (for example, ϵ Indi AB; Dieterich et al. 2018). It is unclear at this point whether this is due to unresolved issues in the models or observational biases. However, in this work, we attempt to derive best-fit fundamental parameters for Gl 229B as well as investigate the plausibility of an anomalously high mass.

2.2. Details on the Primary Gl 229A

In 1995, Nakajima et al. (1995) observed Gl 229A, a known M1V dwarf (Kirkpatrick et al. 1991; Cushing et al. 2006), with the Adaptive Optics Coronagraph at the Palomar 60 inch telescope in search of a proper motion companion. Gl 229A was initially chosen as a target of interest in a search for brown dwarf companions to stars within 15 pc of the Sun. Its known low space motion (Leggett 1992) as well as a precisely measured distance in Hipparcos (Perryman et al. 1997) made it a promising candidate. Since the discovery of Gl 229B, Gl 229A has also been a target of several observational studies, in an attempt to further our understanding of the physics of low mass stars and the fundamentals of this system in particular. However, there are still seemingly discordant conclusions on its age and chemical composition which have added to the mystery of this system as a whole.

Based on its kinematics and coronal activity, it was originally believed to be younger than the Sun, but at least as old as the Hyades (~ 0.8 Gyr), about 0.5–5 Gyr (Nakajima et al. 1995). However, M dwarf ages are notoriously difficult to determine due to the long activity lifetimes of fully convective stars (West et al. 2008). Gl 229A is a prime example of this dilemma, as later studies are in complete disagreement over its age. Leggett et al. (2002a) used evolutionary models from Allard et al. (2001) to argue that its kinematics and flare-star designation support a much younger age of 16–45 Myr. While, more recently, Brandt et al. (2020) used chromospheric and coronal activity, along with gyrochronology relations from

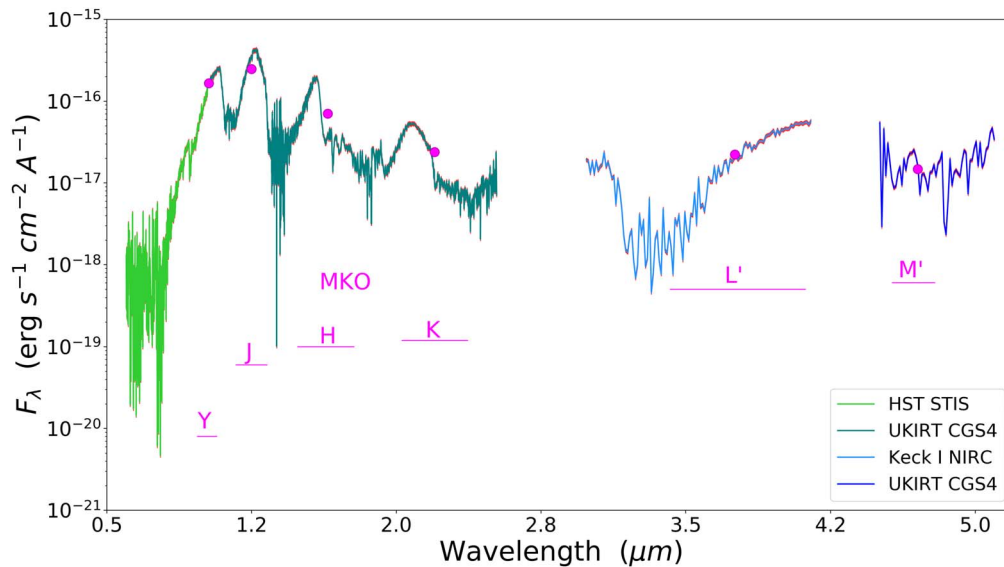


Figure 1. Distanced-calibrated SED for Gl 229B using the spectra listed in Table 2 and photometry listed in Table 1. Spectrum calibration was done using the techniques of Filippazzo et al. (2015), updated with a system parallax measurement from Gaia Collaboration et al. (2021). Pink lines show the wavelength coverage of each photometric band and photometric points are each plotted at their respective band center. Underlying red shows the flux uncertainty which was calculated using $\text{SNR} = 10$.

(The data used to create this figure are available.)

Angus et al. (2019), to estimate an age of 2.6 ± 0.5 Gyr. This is further complicated as Brandt et al. (2020) reports a system age of 7–10 Gyr based on the dynamical mass measurement of Gl 229B. They also calculate an age based on Gl 229A’s membership in the kinematic thin disk, but note that the resulting young age is strongly disfavored by the low levels of chromospheric and coronal activity.

In better agreement among different models are metallicity measurements for Gl 229A. Using medium and high-resolution spectra, Nakajima et al. (2015), Gaidos & Mann (2014), Neves et al. (2014), Mould (1978) and Schiavon et al. (1997) find Gl 229A to be consistent with solar values. There is one exception among the literature which found a best fitting model with $[\text{M}/\text{H}] = -0.5$ (Leggett et al. 2002a). However, spectroscopic measurements do not seem to support such a low metallicity. Reported metallicity measurements for Gl 229A are listed in Table 7. Additionally, Nakajima et al. (2015) reported a C/O ratio for Gl 229A based upon inferred bulk carbon and oxygen abundances published in Tsuji & Nakajima (2014) and Tsuji et al. (2015) and found a slightly supersolar value of 0.68 ± 0.12 (as compared to a solar value of 0.55 from Asplund et al. 2009), making it the only determined C/O ratio for Gl 229A.

2.3. Data Used in Retrievals

For the purposes of this retrieval work, we began using near-infrared data obtained using CGS4 at the United Kingdom 3.8 m Infrared Telescope (UKIRT) (Geballe et al. 1996) whose spectra was updated with improved photometry by Leggett et al. (1999). Table 1 lists the photometry used in this work.

To further constrain the retrieved chemical abundances and other fundamental parameters, L band spectral data from Oppenheimer et al. (1998) and M band spectral data from Noll et al. (1997) were included, making a combined spectral wavelength coverage 1.0–5.0 μm . Table 2 lists the spectra used in this work.

3. Results from the SED

We re-visit the SED in Figure 1, recorded previously in Filippazzo et al. (2015), using the parallax of Gl 229A from the latest Gaia data release, Gaia EDR3 (Gaia Collaboration et al. 2021). As in Filippazzo et al. (2015), both the optical and the infrared spectrum were used to construct the SED. The SED is scaled and distance-calibrated with the available photometry and EDR3 parallax, which we use to find a distance of 5.761 ± 0.001 pc. We follow the exact same methodology as Filippazzo et al. (2015), only updating the SED with this new parallax. The spectra used in the SED are listed in Table 2 while the parallax and photometry are listed in Table 1. The original data did not include a flux uncertainty array so we chose a conservative estimate of $\text{SNR} = 10$ for the entire spectrum.

Bolometric luminosity (L_{bol}) was calculated by integrating under the distance-calibrated SED from 0 to 1000 μm . To account for wavelength coverage gaps in the spectra, the flux in each region was estimated by linearly interpolating to zero from the short wavelength limit and appending a Rayleigh–Jeans tail at the long wavelength limit (Filippazzo et al. 2015). The radius and mass estimates are calculated by comparison to evolutionary models using the derived L_{bol} value and object age. We conservatively assume an object age of between 0.5 and 10 Gyr, since there are no obvious spectral signatures of youth. The range of predicted radius and mass values comes from both the cloudy and cloudless evolutionary models of Saumon & Marley (2008) and Baraffe et al. (2003). The range of values were taken to be the minimum and maximum from all model predictions. The effective temperature, T_{eff} , was calculated by the Stefan-Boltzmann law, using the predicted radius and derived L_{bol} . For a more detailed explanation of the methodology used in the construction of this SED or its derived parameters, see Filippazzo et al. (2015). Fundamental parameters derived from the SED are listed in Table 1 as well as Table 6.

Table 1
Properties of Gliese 229B

Parameter	Value	Reference
Spectral Type	T7p	2
Astrometry		
R.A.	06 ^h 10 ^m 34 ^s .61	1
decl.	− 21 ^h 51 ^m 52 ^s .66	1
π (mas)	173.57 \pm 0.017	1
μ_α (mas yr ^{−1})	−135.692 \pm 0.011	1
μ_δ (mas yr ^{−1})	−719.178 \pm 0.017	1
Photometry		
Y_{MKO} (mag)	15.17 \pm 0.1	3
J_{MKO} (mag)	14.01 \pm 0.05	4
H_{MKO} (mag)	14.36 \pm 0.05	4
K_{MKO} (mag)	14.36 \pm 0.05	4
L'_{MKO} (mag)	12.24 \pm 0.05	5
M'_{MKO} (mag)	11.74 \pm 0.11	5
SED-Derived Parameters		
Radius (R_{Jup})	0.94 \pm 0.15	6
Mass (M_{Jup})	41 \pm 24	6
log(g)	4.96 \pm 0.46	6
T_{eff} (K)	927 \pm 79	6
log($L_{\text{Bol}}/L_{\text{Sun}}$)	−5.21 \pm 0.05	6

References. (1) Gaia Collaboration et al. (2021), (2) Burgasser et al. (2006), (3) Hewett et al. (2006), (4) Leggett et al. (2002b), (5) Golimowski et al. (2004), (6) Filippazzo et al. (2015).

4. Brewster Framework

The retrieval models presented here were constructed with the Brewster retrieval framework (Burningham et al. 2017, 2021). In this section, we provide a brief summary of Brewster as well as any modifications made for this work. We differ from Burningham et al. (2017, 2021) with the use of a version update that utilizes nested sampling via PyMultiNest (Buchner 2014) instead of EMCEE (Foreman-Mackey et al. 2013). For a more detailed description of this framework with a focus on the EMCEE sampler, see Burningham et al. (2017).

4.1. Forward Model

The forward model consists of the radiative transfer solver, thermal profile, and opacity and scattering properties as a function of wavelength. The forward model solves for emergent flux from radiative transfer using the two stream technique of Toon et al. (1989). This includes scattering, first introduced by McKay et al. (1989) and later used by Marley et al. (1996); Saumon & Marley (2008) and Morley et al. (2012). We use a 64 pressure layer atmosphere (65 levels) with geometric mean pressures in range $-4 < \log P < 2.3$ in bars, spaced at 0.1 dex intervals.

4.1.1. Thermal Profile

The thermal profile used is a computationally simple five point parameterization in which we specify five temperature-pressure points: the top (T_{top}), bottom (T_{bottom}) and middle of the atmosphere (T_{middle}) and two midpoints between the top and middle (T_{q1}), and bottom and middle (T_{q3}). These points are calculated in order, beginning with T_{bottom} , which is

selected in range between zero and the maximum temperature defined in our prior. This work defines a maximum temperature of 4000 K. Then T_{top} is chosen between zero and T_{bottom} , T_{middle} chosen between T_{top} and T_{bottom} , and the remaining two midpoints chosen between T_{top} and T_{middle} (T_{q1}), T_{middle} and T_{bottom} (T_{q3}). A uniform prior is assumed for each temperature within its respective range. This does not allow for temperature inversions but can result in “wobbly” profiles.

4.1.2. Gas Opacities

For the models presented in this work, we assume uniform-with-altitude mixing ratios for absorbing gases and calculate layer optical depths using high-resolution ($R = 10,000$) opacities from Freedman et al. (2008, 2014).

Particularly important in the cooler atmospheres of brown dwarfs are the D resonance doublets of Na I ($\sim 0.59 \mu\text{m}$) and K-I ($\sim 0.77 \mu\text{m}$) that create a defining spectral feature in the range 0.4–1.0 μm . In T dwarfs, these line profiles can be detected up to $\sim 3000 \text{ cm}^{-1}$ from the line center (e.g., Burrows et al. 2000; Liebert et al. 2000; Marley et al. 2002; King et al. 2010), making the Lorentzian line profile insufficient. Instead, we implement line wing profiles based on the unified line shape theory (Allard et al. 2007a, 2007b). In previous retrieval work with T dwarfs, Line et al. (2017) suggested the use of alkali opacities from Burrows & Volobuyev (2003) that calculate absorption line profiles for the D1 and D2 lines of Na I and K-I broadened by H₂ - and He collisions for effective temperatures below 2000 K and perturber densities derived from the quasi-static theory of absorption (Holtsmark 1925; Holstein 1950). However, Gonzales et al. (2020) showed that there may not be a clear distinction in preferred tabulated line profiles for T dwarfs between those from Burrows & Volobuyev (2003) and Allard N. (private communication). Broadened D1 and D2 line profiles from Allard N. are calculated for temperatures in the range 500–3000 K and perturber densities up to 10^{20} cm^{-3} , where two collisional geometries are considered for broadening by H₂. Profiles within 20 cm^{-1} of the line center are Lorentzian with a width calculated from the same theory.

Line opacities are tabulated across the temperature-pressure regime in 0.5 dex steps for pressure and in steps from 20 to 500 K for the temperature range 75–4000 K. This is then linearly interpolated to our working pressure grid. We also include Rayleigh scattering for H₂, He, and CH₄ only. We assume atmospheric proportions of 0.84 H₂+0.16 He based on Solar abundances to give an effective broadening width for each line. After retrieving the abundances of the gases assumed to be in the atmosphere, neutral H, H₂ and He are assumed to make up the remainder of the gas in a layer.

4.1.3. Gas Abundances

As stated in the previous section, we assume uniform-with-altitude mixing ratios, as opposed to layer-by-layer varying gas mixing ratios, for all absorbing gases and retrieve the overall abundances directly for all models in this work. It should be noted that the uniform-with-altitude mixing method is a simplification in our model that cannot distinguish variations in gas abundance with altitude for some species, particularly the alkalis, which can vary by several orders of magnitude in the photosphere, or CO, which is believed to be in chemical disequilibrium in the photosphere (Fegley & Lodders 1996; Oppenheimer et al. 1998). However, we utilize the

Table 2
Data Used in Retrieval Models and SED

Wavelength Coverage	Instrument	Resolving Power	Reference	Use
0.5–1.023 μm	HST STIS	$R \sim 500$	Schultz et al. (1998)	SED
1.024–2.52 μm	CGS4 on UKIRT	$R \sim 390\text{--}780\times\lambda$	Geballe et al. (1996)	Retrieval, SED
2.98–4.15 μm	NIRC on Keck I	$R \sim 150$	Oppenheimer et al. (1998)	Retrieval, SED
4.5–5.1 μm	CGS4 on UKIRT	$R \sim 400\times\lambda$	Noll et al. (1997)	Retrieval, SED

uniform-with-altitude method because the layer-by-layer approach is computationally prohibitive.

4.1.4. Cloud Modeling

The cloud parameterizations we utilize in this work closely follow the methodology described in Burningham et al. (2017) and Gonzales et al. (2020, 2021). As in Burningham et al. (2017, 2021), we define two categories of clouds, “slab” and “deck.” Both slab and deck clouds have an opacity distributed among layers in pressure space and an optical depth determined by cloud designation as either gray or non-gray. Total optical depth (τ_{cloud}) for a gray cloud model is calculated at 1 μm . For a non-gray cloud application, we use a power-law distribution to describe the optical depth, $\tau = \tau_0 \lambda^\alpha$, where τ_0 is the optical depth at 1 μm . For the case of a non-gray cloud, we designate another model parameter, the power (α) in the optical depth. We discuss a cloud’s optical depth in terms of extinction and assume an absorbing cloud by setting the single scattering albedo to zero, as done in Gonzales et al. (2020, 2021).

Beyond the gray and non-gray cloud parameterizations, we follow the work of Burningham et al. (2021) by testing different condensate species under the assumption of Mie scattering. In particular, we investigate the impact of zinc sulfide (ZnS) and potassium chloride (KCl) condensates using refractive indices from Wakeford & Sing (2015) and pre-tabulated Mie coefficients as a function of particle radius and wavelength. Wavelength-dependent optical depths and phase angles in each pressure layer are calculated by integrating the cross-sections and Mie efficiencies over the particle size distribution in that layer for a given cloud species. Particle number density in a layer is calibrated to the optical depth at 1 μm as determined by the cloud type (slab or deck). We assume either a Hansen (Hansen 1971) or lognormal distribution of particle sizes. The Hansen distribution for particle number n with radius r is given as:

$$n(r) \propto r^{\frac{1-3b}{b}} e^{-\frac{r}{ab}}, \quad (1)$$

where a and b are the effective radius and spread of the distribution, respectively. These parameters are defined as:

$$a = \frac{\int_0^\infty r \pi r^2 n(r) dr}{\int_0^\infty \pi r^2 n(r) dr}, \quad (2)$$

$$b = \frac{\int_0^\infty (r - a)^2 \pi r^2 n(r) dr}{a^2 \int_0^\infty \pi r^2 n(r) dr}. \quad (3)$$

A deck cloud is parameterized by the cloud top pressure, P_{top} , the decay height, $\Delta \log P$ and the cloud particle single scattering albedo, which we set to zero. The cloud top pressure is defined as the point in pressure space at which the optical depth passes unity, or $\tau = 1$ (looking down). The decay scale pressure describes how the optical depth changes with

changing pressure from the cloud deck and is defined as $d\tau/dP \propto \exp((P - P_{\text{deck}})/\Phi)$, where P_{deck} is the height at which the cloud is optically thick and $\Phi = P_{\text{top}}(10^{\Delta \log P} - 1)/10^{\Delta \log P}$ is the decay scale of the cloud in bars. The deck cloud becomes optically thick at P_{top} , so for $P > P_{\text{top}}$, optical depth increases following the decay function until it reaches $\Delta \tau_{\text{layer}} = 100$. The deck cloud becomes opaque with increasing pressure relatively quickly as a result of the decay function, so we obtain little atmospheric information from deep below the cloud top. To account for this, the pressure-temperature (P-T) profile below the cloud deck is an extension of the gradient and spread at the cloud top pressure.

The distinguishing marker for a slab cloud is the addition of another parameter to determine the total optical depth at 1 μm (τ_{cloud}), since we can “see” the bottom of this type of cloud. The optical depth is distributed throughout the cloud as $d\tau/dP \propto P$ (looking down), where its maximum value is reached at the bottom of the slab (highest pressure). In principle, the slab can have any optical depth, but we restrict the prior to $0.0 \leq \tau_{\text{cloud}} \leq 100.0$. Instead of considering the decay scale pressure, as we did for a deck cloud, we consider the cloud thickness in $d \log P$ and parameterize for cloud top pressure, P_{top} .

4.2. Retrieval Model

The retrieval process depends on the chosen elements of the parameter set. Changing the elements that are passed to the forward model have effects on the resultant spectrum. Optimizing the forward model’s fit to the data by varying the parameter set, or state-vector, takes place within a Bayesian framework. A detailed explanation of this framework can be found in Burningham et al. (2017). To summarize, Brewster applies Bayes’ theorem to calculate the “posterior probability,” $p(\mathbf{x}|\mathbf{y})$, the probability of a set of parameters’ (\mathbf{x}) truth value given some data (\mathbf{y}), in the following way:

$$p(\mathbf{x}|\mathbf{y}) = \frac{\mathcal{L}(\mathbf{x}|\mathbf{y})p(\mathbf{x})}{p(\mathbf{y})}, \quad (4)$$

where $\mathcal{L}(\mathbf{x}|\mathbf{y})$ is the likelihood that quantifies how well the data match the model, $p(\mathbf{x})$ is the prior probability on the parameter set and $p(\mathbf{y})$ is the probability of the data marginalized over all parameter values, also known as the Bayesian evidence. As detailed in Burningham et al. (2017), the original version of Brewster uses EMCEE (Foreman-Mackey et al. 2013) to sample posterior probabilities and inflate errors using a tolerance parameter to allow for unaccounted sources of uncertainty. The EMCEE chain requires tens of thousands of iterations over hundreds of parallel walkers in order to converge and can often require several days of computing to complete a single round of parameter estimation, depending on wavelength range and model complexity. Additionally, the use of EMCEE as a

Table 3
Priors for GI 229B Retrieval Models

Parameter	Prior
gas volume mixing ratio	uniform, $\log f_{\text{gas}} \geq -14$, $\sum_{\text{gas}} f_{\text{gas}} \leq 1$
thermal profile (T_{bottom} , T_{top} , T_{middle} , T_{q1} , T_{q3})	uniform, $0 \text{ K} < T < 4000 \text{ K}$
radius	uniform, $0.5R_{\text{Jup}} \leq R \leq 2.0R_{\text{Jup}}$
mass ^a	uniform, $1M_{\text{Jup}} \leq M \leq 80M_{\text{Jup}}$
cloud top ^b	uniform, $-4 \leq \log P_{\text{CT}} \leq +2.3$
cloud decay scale ^c	uniform, $0 < \log \Delta P_{\text{decay}} < 7$
cloud thickness ^d	uniform, $\log P_{\text{CT}} \leq \log(P_{\text{CT}} + \Delta P) \leq 2.3$
cloud total optical depth (extinction)	uniform, $0 \leq \tau_{\text{cloud}} \leq 100$
single scattering albedo	constant, $\omega_0 = 0$
wavelength shift	uniform, $-0.01 < \Delta\lambda < 0.01 \mu\text{m}$
tolerance factor	uniform, $\log(0.01 \times \min(\sigma_i^2)) \leq b \leq \log(100 \times \max(\sigma_i^2))$

Notes.

^a This mass prior range was constrained to 70–72 M_{Jup} for a single, cloudless model. See Section 5.2.

^b For a deck cloud, this is the pressure where $\tau_{\text{cloud}} = 1$, for a slab cloud this is the top of the slab.

^c Decay height for cloud deck above the $\tau_{\text{cloud}} = 1.0$ level.

^d Thickness and τ_{cloud} retrieved only for slab cloud.

sampler can result in models with degenerate parameter solutions or local, rather than global, maximum likelihoods.

In this new instance of Brewster, the posterior probability space is explored using the PyMultiNest sampler (Buchner 2014; Feroz et al. 2011) which utilizes nested sampling to discover the set of parameters with the maximum likelihood given the data. PyMultiNest is a Bayesian inference tool that explores the parameter space to maximize the likelihood of the forward model fit to the data. The samples in an n -dimensional hypercube, or state-vector, are translated into parameter values via the “prior-map.” The prior-map function is how prior probabilities are set for each parameter and are then transformed into appropriate parameter values to be used in the forward model. This algorithm is equipped to handle a parameter space that may contain multiple posterior modes and/or degeneracies in moderately high dimensions.

Unlike the procedure in Burningham et al. (2017), we retrieve radius and mass directly which are then used to numerically determine a value for gravity. The radius is determined from the scaling factor required to match the absolute flux from the forward model to the data and the measured parallax. The radius is restricted to be within the range 0.5–2.0 R_{Jup} and the mass between 1 and 80 M_{Jup} as suggested by Saumon & Marley (2008), COND (Baraffe et al. 2003) and DUSTY (Chabrier et al. 2000; Baraffe et al. 2002) substellar evolutionary models. In order to investigate a dynamical mass measurement of $71.4 \pm 0.6 M_{\text{Jup}}$ (Brandt et al. 2021), we restrict the probability space for mass to be 70–72 M_{Jup} in just one of our model investigations. Table 3 lists the priors used in our modeling, which are based on those defined in Burningham et al. (2017).

We began this modeling by investigating the impact of running a retrieval model on near-infrared data only (1.0–2.5 μm) as opposed to the entire combined infrared spectrum. We are unable to constrain CO when using only NIR data,

which is known to be in excess of thermo-chemical equilibrium abundance in the photosphere (Oppenheimer et al. 1998). This result is consistent with the work of Line et al. (2015, 2017) which could not constrain CO, CO₂ or H₂S with NIR data, alone. The first observable CO feature in a T dwarf spectrum is expected to be the first vibration-rotation band (1–0) at 4.7 μm which was observationally confirmed in GI 229B by Noll et al. (1997) and then again by Oppenheimer et al. (1998). Therefore, with the addition of extended infrared data (2.98–5.0 μm), we are able to constrain CO abundance across models.

For all models we use the distance-calibrated (to 10 pc) SED beginning at 1.0 μm and out to 5.0 μm . This spectrum calibration differs from the method used in Burningham et al. (2017) in which they calibrated spectra to the 2MASS J -band photometry and used the object’s true distance in their initialization.

We retrieve the following gases known to sculpt T dwarf spectra: H₂O, CO, CH₄, NH₃, Na, and K. We tie Na and K together as a single element in the state vector, assuming a Solar ratio taken from Asplund et al. (2009) (Line et al. 2015; Burningham et al. 2017; Gonzales et al. 2020, 2021). We are consistent with Gonzales et al. (2020) in excluding CO₂ and H₂S from our gas list, as we are still unable to constrain these even with the inclusion of longer wavelength data. We test multiple cloud parameterizations, beginning with the most simple, cloudless model and building to a 5 parameter Mie scattering cloud slab model.

4.3. Model Selection Parameters

Across models, we focused on making changes in our approach to cloud parameterization while holding fixed the gases included in each model, as well as gas abundance method and alkali opacity. In order to compare these different models, we use a calculation of the Bayesian evidence, specifically the logEvidence or logEv, where the highest logEv is preferred. We use the following selection criterion from Kass & Raftery (1995) to distinguish between two models, with evidence against the lower logEv as:

1. $0 < \Delta \log \text{Ev} < 0.5$: no preference worth mentioning
2. $0.5 < \Delta \log \text{Ev} < 1$: positive
3. $1 < \Delta \log \text{Ev} < 2$: strong
4. $\Delta \log \text{Ev} > 2$: very strong

We began by building from the least complex model (cloud-free) to the most complex slab cloud model. We compare Burrows and Allard alkali opacities for the best fit model as there is conflicting evidence over which is preferred for T dwarf retrievals (Line et al. 2017; Gonzales et al. 2020).

5. Retrieval of GI 229B

Table 4 lists all tested models as well as their $\Delta \log \text{Ev}$ relative to the best fit model: the cloudless, Allard alkali model. Based on our selection criterion, it is clear that all models including clouds were strongly rejected, all with $\Delta \log \text{Ev}$ greater than 2, suggesting that no cloud model can provide a strong fit to the spectroscopic features observed in GI 229B. Additionally, we show that a cloudless model using Burrows alkalis is also strongly rejected as compared to cloudless with Allard alkalis. We also list the cloudless model with a mass prior which shows a $\Delta \log \text{Ev}$ that is positively preferred over our best fit cloudless model. However, since we tightly restrict

Table 4
Model Selection for Gliese 229B

Model	Alkali	Number of Parameters	$\Delta\log$ Evidence
Cloudless	Allard	18	0
Grey Deck Cloud	Allard	20	8.78
Grey Slab Cloud	Allard	21	12.72
Power Law Deck Cloud	Allard	21	13.53
ZnS Deck Cloud	Allard	22	14.33
KCl Slab Cloud	Allard	23	17.61
KCl Deck Cloud	Allard	22	19.41
Power Law Slab Cloud	Allard	22	23.78
ZnS Slab Cloud	Allard	23	30.10
Cloudless	Burrows	18	32.21
Cloudless, Mass Prior	Allard	17	-0.85 ^a

Note.

^a Putting a constraint on mass effectively removes one parameter from the model by increasing model confidence. This is why we see a relative increase in $\log\text{Ev}$ for this model compared to our best fit and why we cannot directly compare this model against any other we have tested. See Section 5.1.

the mass range for this one model, we effectively remove one degree of freedom and expect model confidence to increase as a result. Therefore, we cannot directly compare our mass constrained model against any other models we have tested here.

5.1. Best Fit Model: A Cloudless Atmosphere

5.1.1. Retrieved Gas Abundances and Fundamental Parameters

Figure 2 shows the posterior probability distributions for retrieved gas abundances, mass and radius as well as $\log(g)$, T_{eff} , L_{Bol} , C/O ratio, [M/H], [C/H] and [O/H] from our best fit model, which are calculated based on retrieved quantities. We list the values from Figure 2 in Table 5 for ease of reading.

The derived T_{eff} and $\log(g)$ are calculated from the retrieved radius and mass along with the parallax measurement. The scale factor (R^2/D^2) is calculated from the retrieved radius and parallax. T_{eff} is then determined using this derived scale factor and by integrating the flux in the resultant forward model spectra between 0.6 and 20 μm . We find that our retrieval-based T_{eff} is cooler than the semi-empirical value found from the SED, although the large uncertainty on the SED generated value allows for 1.2 σ agreement. However, this ~ 100 K temperature difference is due to our retrieved radius being $\sim 0.16 R_{\text{Jup}}$ larger than its SED value. Our retrieved radius and mass both agree within 1 σ to the values determined from evolutionary models when generating the SED. Our derived value for $\log(g)$ is also within 1 σ agreement with its SED value. Due to the uncertainty on mass being relatively large for both our retrieval model and the SED generated value, as well as inconsistency with the reported dynamical mass, we discuss this fundamental parameter in greater detail in Section 6.1.

The C/O ratio is calculated under the assumption that all of the oxygen exists in H₂O and CO and all of the carbon exists in CO and CH₄. The following equations were used to derive a value for metallicity, [M/H]:

$$f_{\text{H}_2} = 0.84 \times (1 - f_{\text{gas}}) \quad (5a)$$

$$N_{\text{H}} = 2f_{\text{H}_2} N_{\text{tot}} \quad (5b)$$

$$N_{\text{element}} = \sum_{\text{molecules}} n_{\text{atoms}} f_{\text{molecule}} N_{\text{tot}} \quad (5c)$$

$$N_M = \sum_{\text{element}} \frac{N_{\text{element}}}{N_{\text{H}}} \quad (5d)$$

$$[M/H] = \log\left(\frac{N_M}{N_{\text{Sun}}}\right) \quad (5e)$$

where f_{H_2} is the fraction of H₂, f_{gas} is the total gas fraction, N_{H} is the number of neutral hydrogen atoms, N_{element} is the number of atoms for each element, n_{atoms} is the number of atoms for a given element contained in a single molecule and N_{tot} is the total number of gas molecules. In our calculation of metallicity, N_{Sun} is determined using the same formula as N_M , using the sum of the solar abundances compared to H. Both [C/H] and [O/H] were calculated using the same procedure for total metallicity using just single element abundances.

As we do not have an SED-based comparison for C/O ratio or metallicity, we discuss these parameters in greater detail in Section 8.

5.1.2. Temperature–Pressure Profile, Contribution Function and Abundances

Figure 3(a) shows the retrieved temperature versus pressure (T-P) profile for the best fit cloudless model for Gl 229B. Overplotted in this figure are the Sonora grid models (Marley et al. 2021) using Solar-metallicity. The slight thermal inversion apparent in the very top of the atmosphere (~ 0.01 – 0.001 bar) in our retrieved profile is a computational consequence of our initialized five point profile and not thought to actually exist in that way. As a result, we have much larger 1 σ and 3 σ confidence ranges in that pressure space. Our retrieved profile is in best agreement with the Sonora Solar-metallicity $\log(g) = 5.0$, 850 K model throughout the photosphere (~ 0.5 – 20 bar). While the 1 σ and 3 σ bounds are relatively small in this pressure range, the $\log(g) = 5.0$, 850 K model fits the profile almost entirely within these bounds. This model agrees to within 3 σ in the upper atmosphere, as well. Comparing our retrieved profile to the Solar-metallicity $\log(g) = 5.0750$ K model, our profile is ~ 50 K warmer throughout most of the photosphere, although we do see 1 σ agreement at the top of the atmosphere (≤ 0.3 bar) as well as at the bottom of the photosphere. For the $\log(g) = 5.0$, 950 K model, it is clear that our profile is at least 100 K cooler throughout the photosphere and deeper into the atmosphere.

Figure 3(b) shows the contribution function indicating the location of an optical depth of $\tau = 1$ for the gas opacity. The contribution function is calculated in each pressure layer in the following way:

$$C(\lambda, P) = \frac{B(\lambda, T(P)) \int_{P_1}^{P_2} d\tau}{e^{\int_{P_0}^{P_2} d\tau}}, \quad (6)$$

where $B(\lambda, T(P))$ is the Planck function, P_0 is the pressure at the top of the atmosphere, P_2 is the pressure at the bottom of the layer and P_1 is the pressure at the top of the layer. The majority of the flux in the near-infrared spans a relatively large portion of the atmosphere from ~ 0.5 to 80 bar compared to the flux contribution in the early mid infrared that originates higher in the photosphere around ~ 0.2 –15 bar.

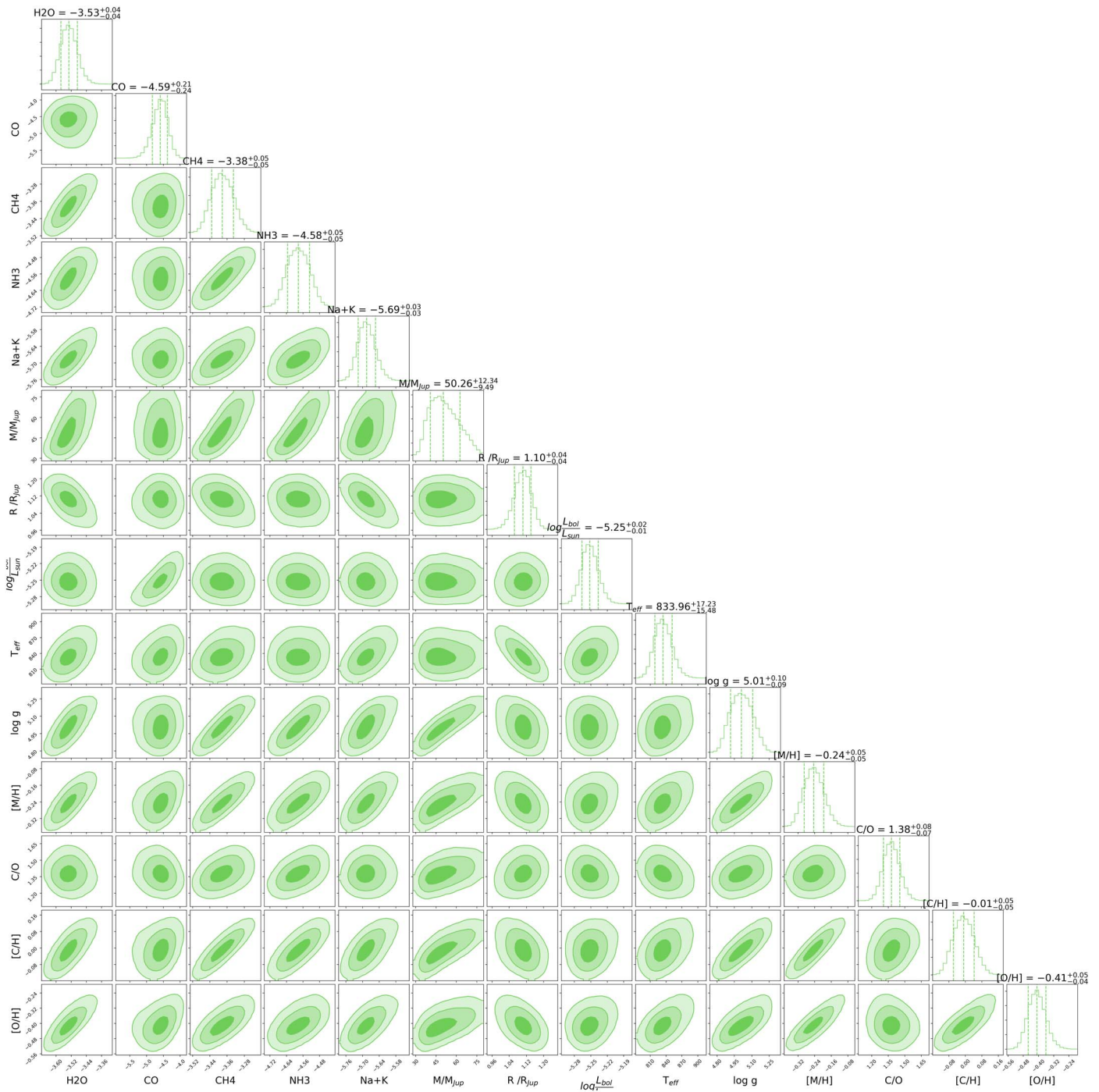


Figure 2. Best Fit Model: Cloudless, Allard Alkalies Posterior probability distributions for retrieved gas abundances, mass, radius and derived quantities of the best fit cloudless model with Allard alkalies. Far right diagonal plots show marginalized posteriors for each parameter along with 2D parameter correlation histograms. Dashed lines show the median retrieved value (reported value) along with 1σ confidence intervals. Gas abundances are in units of dex.

Figure 3(c) shows retrieved gas abundances as compared to thermo-chemical equilibrium grid model abundances. These chemical grids were calculated using the NASA Gibbs minimization CEA code (McBride & Gordon 1994) based on prior thermo-chemical models (Fegley & Lodders 1994, 1996; Lodders 1999, 2002, 2004, 2010; Lodders & Fegley 2002, 2006; Visscher et al. 2006, 2010; Visscher 2012; Moses et al. 2012, 2013). These grids are then used to determine thermo-chemical equilibrium abundances of various atmospheric species for pressure in the range 1 microbar – 300 bar and temperatures in the range 300–4000 K. In this case, we

compare against chemical grids of Solar metallicity and supersolar C/O ratio of 1.0 relative to the Asplund et al. (2009) Solar value of 0.55.

Since our model calculates uniform-with-altitude abundances, as opposed to the more physically plausible varying-with-altitude mixing ratios (see Section 4), our retrieved values for CO and Na+K show the median retrieved abundance despite their equilibrium abundances trailing off toward lower values at the top of the photosphere. This retrieved abundance can be considered an average of abundances probed at different pressure levels in the photosphere. Therefore, we expect to find

Table 5
Cloudless, Allard Alkali Model Parameters

Parameter	Value	
Model	Best Fit ^a	Mass Constrained ^b
Retrieved		
H ₂ O	-3.53 ± 0.04	-3.49 ± 0.03
CO	$-4.59_{-0.24}^{+0.21}$	$-4.56_{-0.25}^{+0.22}$
CH ₄	-3.38 ± 0.05	-3.32 ± 0.03
NH ₃	-4.58 ± 0.05	-4.51 ± 0.03
Na+K	-5.69 ± 0.03	-5.67 ± 0.03
Radius (R_{Jup})	1.10 ± 0.04	1.12 ± 0.04
Mass (M_{Jup})	50_{-9}^{+12}	71 ± 1
Derived		
log g (dex)	$5.01_{-0.09}^{+0.10}$	5.15 ± 0.03
T_{eff} (K)	834_{-15}^{+17}	829_{-17}^{+19}
$\log(L_{\text{Bol}}/L_{\text{Sun}})$	$-5.25_{-0.01}^{+0.02}$	$-5.25_{-0.01}^{+0.02}$
C/O	$1.38_{-0.07}^{+0.08}$	1.45 ± 0.07
C/O ^c	$1.06_{-0.05}^{+0.06}$	$1.11_{-0.05}^{+0.06}$
[M/H]	-0.24 ± 0.05	-0.19 ± 0.03
[C/H]	-0.01 ± 0.05	0.05 ± 0.03
[O/H]	$-0.41_{-0.04}^{+0.05}$	-0.37 ± 0.04

Notes.

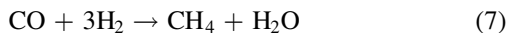
^a Best fit model without any prior constraints placed on retrieved parameters.

^b Best fit model with a prior constraint placed on the mass.

^c Oxygen-corrected C/O ratio (see Section 8).

a median retrieved abundance close to the expected value in the middle of the photosphere. More generally, we would at least expect the retrieved abundance to be within the range of top-of-atmosphere and bottom-of-atmosphere abundances set by the thermo-chemical equilibrium grids. Here, we can see photo-spheric agreement around 10 bar for CO and 3 bar for Na+K. A similar result is shown for NH₃ where the median retrieved abundance is in range of its equilibrium abundance in the photosphere.

There is a distinction for our retrieved H₂O and CH₄ which show a slightly depleted abundance as compared to their equilibrium predictions. H₂O, CH₄ and CO are plotted together in Figure 3(c) as their chemical mixing influences the photospheric abundances we observe. We know from Oppenheimer et al. (1998) and Noll et al. (1997) that there are unexpectedly high amounts of CO in the atmosphere of Gl 229B based on spectral features, particularly at 4.7 μm , which suggest disequilibrium chemistry. A slightly depleted abundance of H₂O and CH₄ could be a result of strong vertical mixing that also causes CO abundance in excess of thermo-chemical equilibrium predictions in the photosphere. This is due to mixing timescales being shorter than the CO \rightarrow CH₄ chemical timescale (Fegley & Lodders 1996; Marley & Robinson 2015), where the net reaction for this conversion in Gl 229B is



(Visscher & Moses 2011). We discuss further causes for depleted oxygen abundance in Section 8. In general, since we expect chemical disequilibrium in the atmosphere of Gl 229B and we are freely retrieving gas abundances (as opposed to retrieving thermo-chemical equilibrium abundances), it is not surprising that our abundances for H₂O and CH₄ differ slightly from these chemical grids.

5.1.3. Retrieved Spectrum versus Forward Model Fit

Figures 4(a) and (b) show our retrieved spectrum as compared to the observed data. The retrieved spectrum fits the near-infrared portion of the observed spectrum well, even though it struggles to reach the top of the flux peaks in the J and H spectral bands. The retrieved spectrum is able to fit the methane features at 1.63, 1.67 and 1.71 μm particularly well. It also fits the narrow absorption features due to water on the shortward side of the H -band peak. There is also a good fit to the top of the flux peak in the K -band. The choice of alkalis had a significant impact on how our model fit the K-I doublet in the J spectral band. In particular, we find the use of Allard alkalis fits this K-I doublet much better than a cloudless model with Burrows alkalis. This difference in the retrieved spectrum J -band between the Allard and Burrows cloud models is likely a result of how pressure broadening for these lines is calculated for objects in this temperature regime. The retrieved spectrum does a good job of fitting the fundamental methane absorption feature of the L spectral band, particularly in the region from 3.6 to 4.1 μm . The retrieved spectrum also fits the general shape of the M spectral band data and attempts to fit the CO feature at 4.67 μm , providing a generally good fit within uncertainty bounds. This could be due to difficulty fitting disequilibrium abundances of CO, as CO is also the most poorly constrained of all the gases in our model. It is important to note that the narrow feature around $\sim 4.8 \mu\text{m}$ is due to an incorrect removal of a telluric line (Noll et al. 1997) and therefore we do not expect our model to fit this.

Figures 4(c) and (d) show our retrieved spectrum and observed data in comparison to Sonora model synthetic spectra that bracket our retrieved T_{eff} . We find that the observed spectrum is best fit by the 850 K Solar metallicity model, overall, but note that it does not reach the flux peak in the L -band. We also point out that none of the Sonora models seem to adequately fit the observed M -band data. While model spectra can provide good spectral fits in certain bands, no single model can simultaneously fit J , H , K , L and M spectral bands as well as our best fit retrieval model spectrum.

5.2. Best Fit Model with a Mass Constraint

In this section, we present results from constraining the posterior probability range for the mass from 10–80 M_{Jup} to 70–72 M_{Jup} on our best fit model. The motivation for placing a prior on this model is the dynamical mass reported in Brandt et al. (2021) that predicts a companion mass for Gl 229A of $71.4 \pm 0.6 M_{\text{Jup}}$. Placing a prior on the model inherently increases model confidence, so we do not use our Bayesian evidence parameter to compare with our best fit model (i.e., retrieval model without prior knowledge placed on retrieved parameters). However, we intend to use this model constraint to compare retrieved gas abundances and fundamental parameters to our best fit model, in order to understand whether the photospheric chemistry can be explained by a 70 M_{Jup} object as well as a 50 M_{Jup} object in Section 6.1.

5.2.1. Retrieved Gas Abundances and Fundamental Parameters

Figure 5 shows the posterior probability distributions for retrieved gas abundances and radius in addition to the derived $\log(g)$, T_{eff} , L_{Bol} , C/O ratio, [M/H], [C/H] and [O/H] for the mass constrained model. We list the values from Figure 5 in Table 5 for ease of reading.

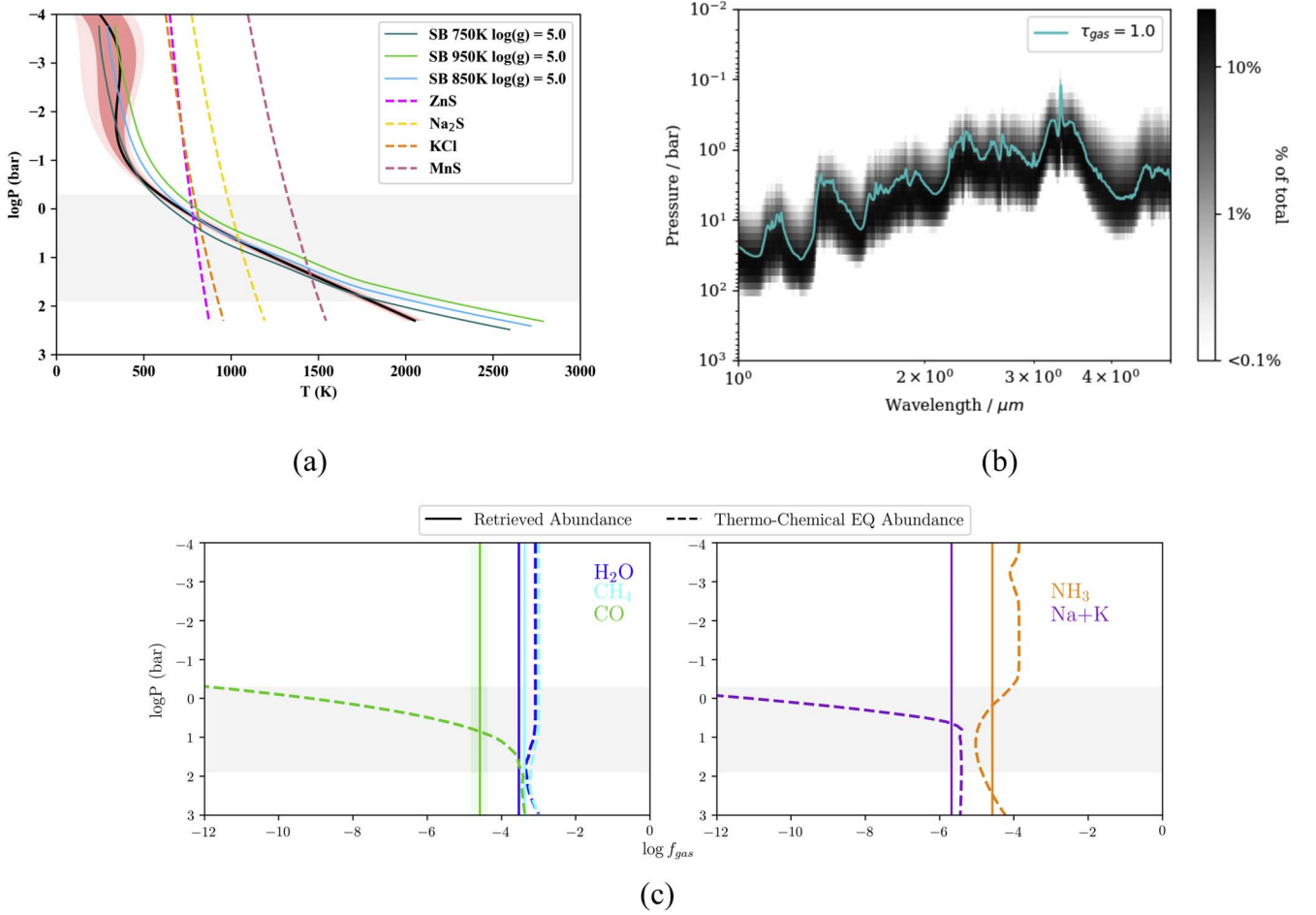


Figure 3. Best Fit Model: Cloudless, Allard Alkalies Figures on the top line show (a) retrieved temperature–pressure profile and (b) contribution function for the best fit model. Our maximum likelihood retrieved profile is shown in black compared to the cloudless Sonora Solar model profiles (green and blue) at similar temperature to our retrieved T_{eff} . Dashed lines show condensation curves for possible cloud species. In the bottom panel (c) we show retrieved uniform-with-altitude mixing abundances as compared to thermo-chemical equilibrium grid abundances for supersolar C/O (1.0 relative to 0.55 of Asplund et al. 2009) and Solar metallicity. In both figures (a) and (c), we show the approximate location of the photosphere as determined by our contribution function with the inclusion of a light gray panel. (The data used to create this figure are available.)

The procedure to calculate T_{eff} , $\log(g)$, C/O ratio and metallicity are described in Section 5.1. Again, we have 1σ agreement with the retrieved radius and derived $\log(g)$ to the values determined from the SED. The mass constrained model found a T_{eff} slightly cooler than the best fit model, however, we still have agreement within 1.2σ to the SED value.

As compared to parameters of the best fit model, the T_{eff} , radius, and $\log(L_{\text{Bol}}/L_{\text{Sun}})$ of the constrained model are all within 1σ agreement. We have 1.5σ agreement with $\log(g)$ values which is expected considering the higher mass of the constrained model. Additionally, we have retrieved abundances of H₂O, CO, Na and K in 1σ agreement and CH₄ and NH₃ within 1.5σ agreement between models. For an object of this temperature, we expect to see increased abundance in both CH₄ and NH₃ as a result of an increased $\log(g)$ as compared to CO, for example, which is thought to be less sensitive to gravity (Zahnle & Marley 2014). Overall, we find the chemistry and temperature to be consistent between our best fit, cloudless model and a cloudless model with a constraint at the dynamical mass value.

5.2.2. Temperature–Pressure Profile

Figure 6(a) shows the retrieved T–P profile for the mass constrained cloudless model as compared to our best fit cloudless profile as well as Sonora grid models. As our derived T_{eff} is only slightly cooler (~ 5 K) for this mass constrained model than our best fit model, we find the Sonora Solar-metallicity $\log(g) = 5.0$, 850 K model fits well throughout the top of the photosphere (1–5 bar). At pressures >10 bar and above the photosphere we have better agreement with the 750 K model. The 1σ and 3σ bounds, which were previously noted to be small for the best fit model, are shown to almost disappear below 1 bar. This is due to increased model confidence as a result of the prior constraint placed on mass. However, we still see good agreement to the $\log g = 5.0$, 850 K model throughout the top of the photosphere until about $P = 5$ bar where the Sonora model diverges from our profile to slightly warmer temperatures. Above the photosphere, we have agreement within 3σ to both 750 K and 850 K models. In contrast, the mass constrained model profile is approximately 100 K cooler throughout the photosphere than the Solar-metallicity $\log g = 5.0$, 950 K model.

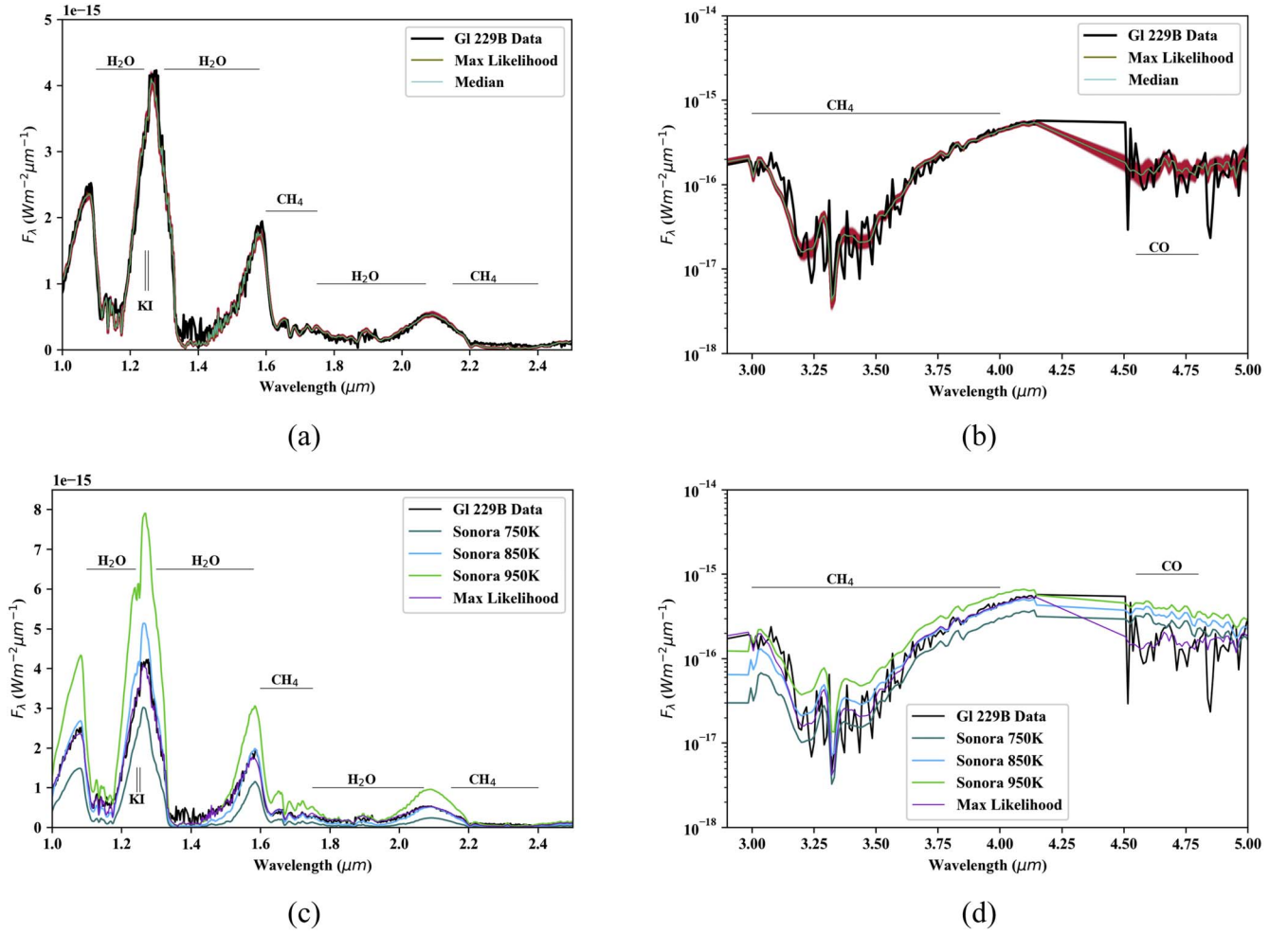


Figure 4. Best Fit Model: Cloudless, Allard Alkalies On top (a) and (b) show the median and maximum likelihood retrieved spectra as compared to observed data for the best model. In red, we show flux uncertainty on this retrieved spectrum. In the bottom panel (c) and (d), we show the maximum likelihood retrieved spectrum and observed spectrum as compared to Sonora grid models of Solar metallicity and C/O at 750, 850, 950 K (blue and green).

(The data used to create this figure are available.)

As shown in Figure 6(a), the best fit profile is nearly identical to the mass constrained profile, only diverging to slightly warmer temperatures (~ 10 K) toward the bottom of the photosphere (around 5 bar).

5.2.3. Retrieved Spectrum versus Best Fit Model

The retrieved spectrum for the mass constrained model is shown in Figures 6(b) and (c). As compared to the spectral fit from our best fit model, a cloudless model with a mass prior around $70 M_{\text{Jup}}$ fits the observed spectrum for Gl 229B just as well. These nearly identical fits show very good agreement throughout the near-infrared and into the *L* and *M* spectral bands with both model spectra being able to fit the notable water, methane and carbon monoxide features. We do note that our mass constrained retrieved spectrum shows a marginally worse fit to the top of the flux peak in the *J* and *H* bands than the best fit retrieved spectrum fit, but maintains a similarly good fit to the top of the flux peak in the *K*-band. The only notable difference between these model fits is the K-I doublet in the *J*-band where the mass constrained model predicts a slightly shallower feature than exists in the observed data. Otherwise, we find a similarly good spectral fit overall.

6. Fundamental Parameter Comparison of Gl 229B

6.1. The Mass of Gl 229B

Of all fundamental parameters to consider, constraining the mass of Gl 229B has been a top priority as an updated dynamical mass of $71.4 \pm 0.6 M_{\text{Jup}}$ reported in Brandt et al. (2021) is at odds with several evolutionary model predictions that placed Gl 229B in the $30\text{--}55 M_{\text{Jup}}$ range (Nakajima et al. 1995, 2015; Allard et al. 1996; Marley et al. 1996). While it is difficult to determine a precise age for Gl 229A, gyrochronology, thin disk kinematics and coronal and chromospheric activity all disfavor an old age, placing the Gl 229 system at an intermediate age of 2–6 Gyr (Brandt et al. 2020). Evolutionary models (ex: Burrows et al. 1997; Allard et al. 2001; Saumon & Marley 2008; Phillips et al. 2020) predict that a T dwarf with a mass of $71.4 \pm 0.6 M_{\text{Jup}}$ would have to be 4–7 Gyr older than the predicted age of Gl 229A to have cooled to an observable $\log(L_{\text{Bol}}/L_{\text{Sun}}) \approx -5.2$. As a result, best fit evolutionary models place Gl 229B at or below $55 M_{\text{Jup}}$ in order to be consistent with this age–mass–luminosity relation. While our best fit model independently deduced a mass of $50^{+12}_{-9} M_{\text{Jup}}$, we also present results using our best fit model (cloudless, Allard

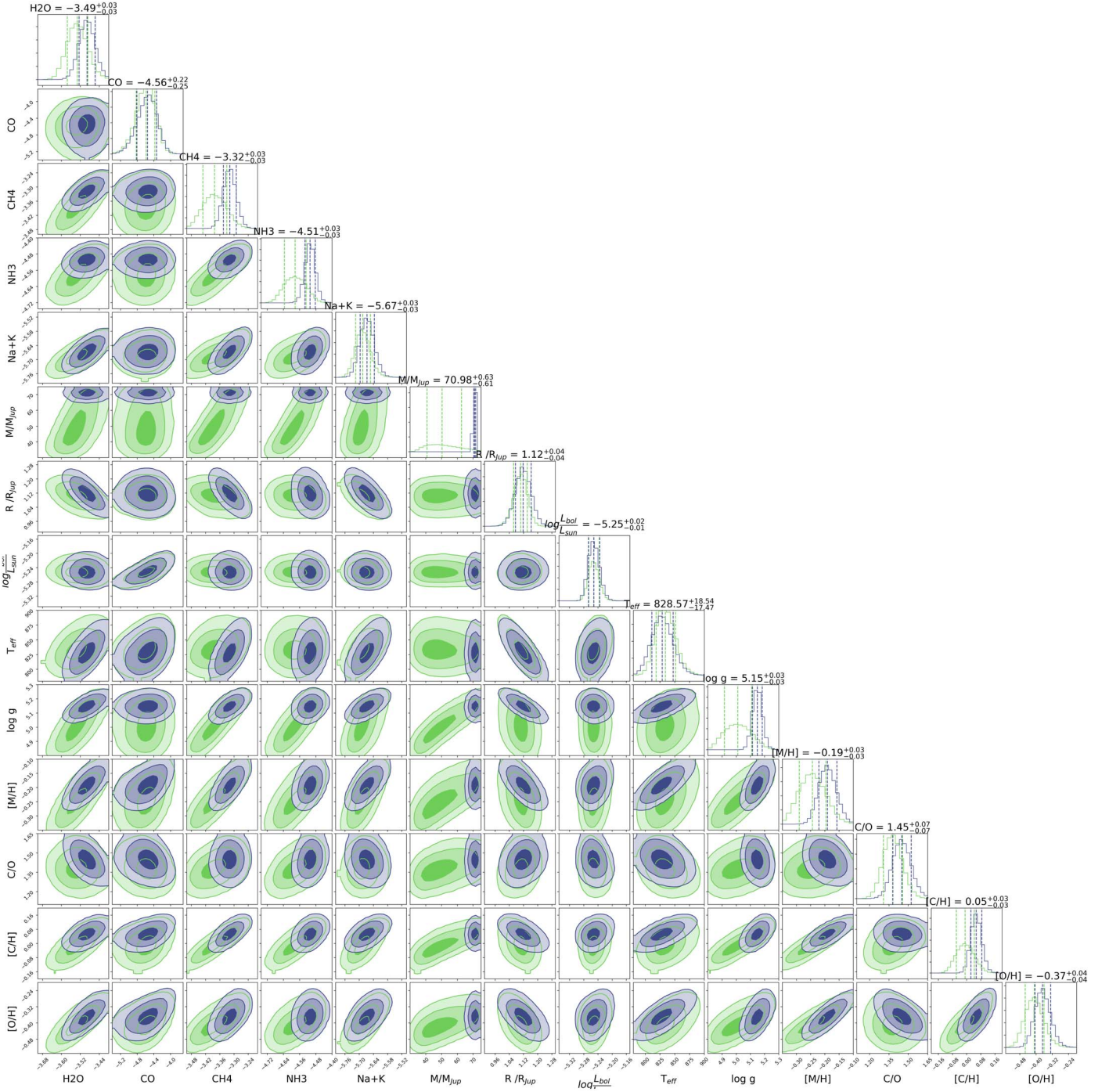


Figure 5. Best Fit Model with a Mass Constraint Posterior probability distributions for retrieved gas abundances and derived fundamental parameters of the mass constrained model shown in blue, as compared to probability distributions from the best fit model (green). As before, marginalized posteriors are plotted on the main diagonal with 2D correlations between each parameters shown. Gas abundances are given in units of dex.

alkalies) with a constraint on the posterior probability space for mass from 1–80 to 70–72 M_{Jup} .

From our results in Section 5.2 with the constrained mass prior, we see an increase in all molecular abundances as compared to our best fit model. However, the abundances of the mass constrained model are all within or close to the 1σ bounds of the best fit model. We find no difference in any retrieved abundance worth mentioning. There is an increase in our calculated $\log(g)$ from $5.01^{+0.10}_{-0.09}$ to 5.15 ± 0.03 which is expected, due to the increased mass. However, we do see a

relative increase in retrieved radius from 1.10 ± 0.04 to $1.12 \pm 0.04 R_{Jup}$ which is unexpected since brown dwarfs are predicted to contract with age. However, these retrieved radii agree within 1σ so while this result is unexpected it is not unreasonable. Retrieved and calculated values for both models are listed in Table 5.

While our model places no constraint on the age of Gl 229B, we present results showing the plausibility that the spectrum and atmospheric chemistry can be fit consistently as well by a 70 M_{Jup} model as it can by a 50 M_{Jup} model.

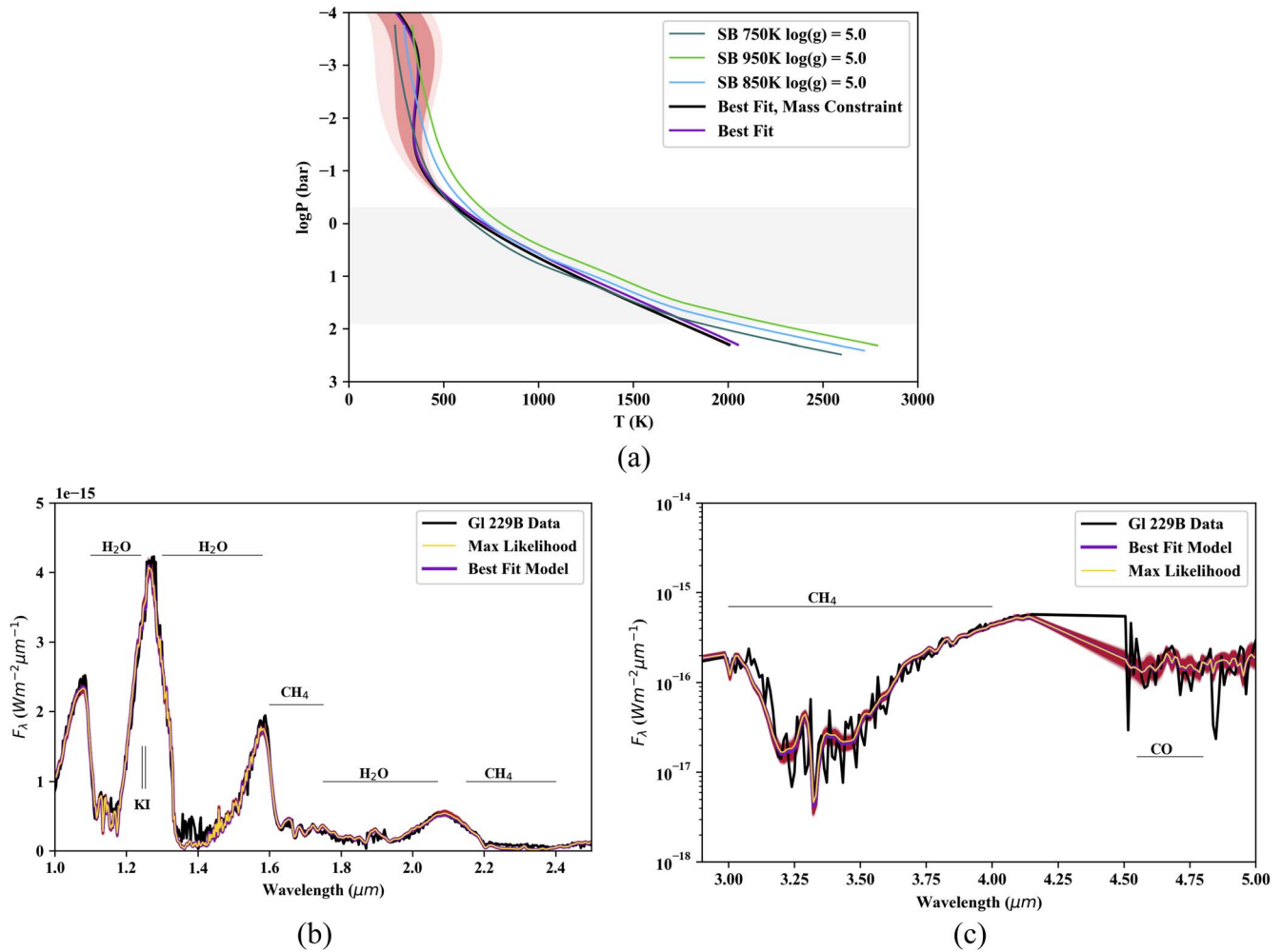


Figure 6. Best Fit Model with a Mass Constraint (a) Retrieved temperature-pressure profile for the mass constrained cloudless model with Allard alkalis as compared against Sonora model profiles (blue and green) and the retrieved profile from our best fit model (purple). Again, we show the approximate location of the photosphere as determined by our contribution function with the inclusion of a light gray panel. Figures (b) and (c) show the maximum likelihood retrieved spectrum for the mass constrained model in yellow compared against observed data (black) and the maximum likelihood retrieved spectrum from the best fit model (purple). In red, we show flux uncertainty on this retrieved spectrum.

6.2. L_{Bol} , Radius, T_{eff} and $\log(g)$ of GJ 229B

In Table 6 we list our SED derived and retrieved fundamental parameters as compared to values from the literature for GJ 229B. We find that our semi-empirical SED derived L_{Bol} , radius, mass and $\log(g)$ agree within 1σ to our best fit model retrieved parameters, while T_{eff} agrees within 1.2σ .

Comparing our retrieval-derived $\log(g)$ to values published in the literature, we find agreement within 1σ between our best fit model and all literature predictions except Leggett et al. (2002a) and Brandt et al. (2020), however, we note that the published $\log(g)$ from Leggett et al. (2002a) is in 2σ disagreement with all other published values due to the young age estimate of the system. Our mass constrained model $\log(g)$ is in agreement within 1σ with Allard et al. (1996) and Saumon et al. (2000) and within 2.5σ to Nakajima et al. (2015). Our constrained model is not in agreement with the reported $\log(g)$ from Brandt et al. (2020), however, the reported uncertainties for both values are notably small.

The T_{eff} we derive for both the best fit and mass constrained model is cooler than all literature values except Nakajima et al. (2015), which agrees within 1σ . We retrieved the same L_{Bol} for

both constrained and best fit models and find its value is slightly smaller than those reported in the literature but still see 2σ agreement to nearly all models, despite small uncertainties.

7. GJ 229B Compared to Other Retrieved T Dwarfs

In this section, we place our best fit retrieval of GJ 229B in context with previous retrieval work on T dwarfs. Initially, Line et al. (2015) presented retrieval results of benchmark T dwarfs GJ 570D and HD 3651B which was later expanded upon in Line et al. (2017) with retrievals of a total of eleven T dwarfs. Zalesky et al. (2019) focused their work on ultra-cool dwarfs with a sample of 14 objects, six of which were late-T type dwarfs, and expanded on this work in Zalesky et al. (2022) with a sample of 50 T7-T9 type dwarfs. Additionally, Kitzmann et al. (2020) presented a retrieval study on the ϵ Indi Bab system, a system with two T-type companions. Finally, we examine our work in context with the retrieval of GJ 229B done by Howe et al. (2022).

Consistent with Line et al. (2015, 2017), we do not include CO₂ or H₂S in our final model since preliminary results showed their abundances to be unconstrained. However, with the use of L and M spectral band data, we are able to put upper and lower

Table 6
Comparison of Fundamental Parameters for Gliese 229B

Source	Radius (R_{Jup})	Mass (M_{Jup})	$\log g$	T_{eff} (K)	$\log(L_{\text{Bol}}/L_{\text{Sun}})$	C/O	[M/H]	Age (Gyr)
This Paper ^a	0.94 ± 0.15	41 ± 24	4.96 ± 0.46	927 ± 79	-5.21 ± 0.05	...	0.0	0.5–10
This Paper ^b	1.10 ± 0.04	50^{+12}_{-10}	$5.01^{+0.10}_{-0.09}$	834^{+17}_{-15}	$-5.25^{+0.02}_{-0.01}$	$1.38^{+0.08}_{-0.07}$	-0.24 ± 0.05	...
This Paper ^c	1.12 ± 0.04	71 ± 1	5.15 ± 0.03	829^{+19}_{-17}	$-5.25^{+0.02}_{-0.01}$	1.45 ± 0.07	-0.19 ± 0.03	...
Naka95	...	20–50	...	<1200	-5.398	0.5–5
Naka15	...	30–38	4.87 ± 0.12	825 ± 25	0.13 ± 0.07	1–2.5
Legg02	...	>7	3.5 ± 0.5	1000 ± 100	-5.21 ± 0.02	...	-0.5	0.016–0.045
Legg99	...	25–35	...	900	-5.18 ± 0.04	0.5–1
Alla96	...	40–58	5.3 ± 0.2	1000	-5.21 ± 0.1	0.5–5
Matt96	913	-5.194
Saum00	...	15–73	5.0 ± 0.5	950 ± 80	-5.21 ± 0.04	...	-0.3 ± 0.2	>0.2
Bran20	...	70 ± 5^d	5.433 ± 0.033	1025 ± 15	-5.208 ± 0.007^e	7–10
Howe22	1.11 ± 0.03	41.6 ± 3.3	$4.93^{+0.02}_{-0.03}$	869^{+5}_{-7}	...	1.13 ± 0.03	-0.07 ± 0.03	...

Notes.^a SED.^b Best Fit Model.^c Mass Constrained Best Fit Model.^d This dynamical mass has since been updated in Brandt et al. (2021) with improved astrometry from Gaia EDR3 (Gaia Collaboration et al. 2021) to be 71.4 ± 0.6 .^e This value is taken from Filippazzo et al. (2015) which we have updated in this work.**References.** Naka95: Nakajima et al. (1995), Naka15: Nakajima et al. (2015), Legg02: Leggett et al. (2002a), Legg99: Leggett et al. (1999), Alla96: Allard et al. (1996), Matt96: Matthews et al. (1996), Saum00: Saumon et al. (2000), Bran20: Brandt et al. (2020), Howe22: Howe et al. (2022).

bound constraints on CO abundance where there previously were none. From the results listed in Table 4, we also find that the data does not justify the addition of an optically thick cloud. We extend this result from Line et al. (2015, 2017) to include optically thin clouds and further confirm that the data does not support the inclusion of condensates in the observable atmosphere as expected for this spectral type (e.g., Gao et al. 2020).

From the sample in Line et al. (2017), we focus our retrieved parameter comparison to objects within 100 K of our retrieved $T_{\text{eff}} = 834^{+17}_{-15}$ K for Gl 229B: 2MASS J00501994 – 3322402 ($T_{\text{eff}} = 815^{+20}_{-27}$ K), 2MASS J0727182 + 171001 ($T_{\text{eff}} = 807^{+17}_{-19}$ K), 2MASS J1553022 + 153236B ($T_{\text{eff}} = 803^{+16}_{-27}$ K) and 2MASS J07290002 – 3954043 ($T_{\text{eff}} = 737^{+21}_{-25}$ K). Our retrieved $\log(g)$ and radius are within 1σ agreement to that of 2MASS J00501994 – 3322402 and 2MASS J0727182 + 171001, only. We have 1σ agreement on retrieved abundances of H₂O and CH₄ for 2MASS J00501994 – 3322402 and H₂O, CH₄ and NH₃ for 2MASS J0727182 + 171001. We retrieve lower abundances of Na and K as compared to both objects which is likely due to the difference in alkali line opacities used in this work than Line et al. (2017).

As the selected T dwarfs in Zalesky et al. (2019) are of type T8 or later, we have no direct comparison to focus on, so we instead turn to Zalesky et al. (2022). We discuss the objects in their sample close in temperature (<50 K difference) to that of our best fit for Gl 229B: WISE J024124.73 – 365328.0 ($T_{\text{eff}} = 836 \pm 4$ K), WISE J112438.12 – 042149.7 ($T_{\text{eff}} = 848^{+26}_{-10}$ K) and WISEPC J221354.69 + 091139.4 ($T_{\text{eff}} = 852^{+12}_{-11}$ K). We have 1σ agreement on the retrieved $\log(g)$ and radius for WISE J024124.73 – 365328.0 and WISE J112438.12 – 042149.7 and 1.2σ agreement with WISEPC J221354.69 + 091139.4. Since Zalesky et al. (2022) independently retrieves abundances for sodium and potassium, instead of tying their abundance ratio to solar value as we do here, we will only compare abundances for the constrained gases they report. While we do see slightly higher abundances of CH₄ and NH₃ in our model as compared to all

three of these objects, we still have 1σ agreement across H₂O, CH₄ and NH₃ abundance for WISE J024124.73 – 365328.0 and WISE J112438.12 – 042149.7. For J221354.69 + 091139.4, we have 1σ agreement with H₂O and CH₄ abundance and 1.2σ agreement with NH₃.

While the ϵ Indi system consists of an early T1.5 and T6 dwarf as a binary companion to a stellar type primary, we note that the T6 dwarf is too warm for a direct chemical comparison to Gl 229B. However, we are consistent with both Zalesky et al. (2019, 2022) and Kitzmann et al. (2020) in reporting cloud-free best fit models. We discuss these retrievals further in Section 8.3 as they relate to developing C/O ratio and metallicity trends in retrieval work.

Finally, we place our Gl 229B retrieval in context with that realized in Howe et al. (2022) which utilizes the same spectrum as we do in this work with the addition of 0.8–1.0 μm optical data from Schultz et al. (1998). This work employs the retrieval code APOLLO (Howe et al. 2017) and uses opacities from Freedman et al. (2014). While Howe et al. (2022) reports uniformly small uncertainties on all retrieved gases and fundamental parameters, we do still have 1σ agreement with our best fit model to the retrieved abundances for CH₄ and NH₃ and retrieved $\log(g)$, radius and mass. We also have 2σ agreement with retrieved temperature. However, we do see disagreement between the retrieved abundances of H₂O, CO and Na+K where our model finds lower abundances for all three parameters on the order of 3σ or greater. This could be due to differences in line lists used in these works as well as differences in underlying assumptions and biases between the two retrieval codes.

8. C/O and Metallicity of Gl 229B

8.1. C/O and Metallicity of Gl 229B as Compared to its Primary

In Table 7, we list reported metallicities for Gl 229A, which, similar to reported values for Gl 229B, range from subsolar to supersolar. For both best fit and mass constrained retrieval

Table 7
Comparison of Fundamental Parameters for Gliese 229A

Source	Radius (R_{Sun})	Mass (M_{Sun})	$\log g$	T_{eff} (K)	$\log(L_{\text{Bol}}/L_{\text{Sun}})$	C/O	[M/H]	Age (Gyr)
Legg02	...	0.30–0.45	3.75 ± 0.25	3700	−1.29	...	-0.6 ± 0.1	0.016–0.045
Moul78	4.75	3610	0.15 ± 0.15	...
Tsuj14	0.496	0.524	4.77	3710
Naka15	4.77	0.68 ± 0.12	0.13 ± 0.07	...
Schi97	4.7	3330	-0.2 ± 0.4^a	...
Gaid14	0.53 ± 0.05	0.56 ± 0.07	...	3800 ± 100	-1.30 ± 0.1	...	0.12 ± 0.10^a	...
Neve14	...	0.58 ± 0.03	...	3630 ± 110	-0.03 ± 0.09^a	...
Bran21	...	0.579 ± 0.007	2.6 ± 0.5^b

Notes.

^a Metallicity reported as [Fe/H].

^b This age value is calculated in Brandt et al. (2020) based on stellar activity, but they adopt a prior age of the system of 1–10 Gyr due to disagreement between the derived stellar and brown dwarf ages.

References. Legg02: Leggett et al. (2002a), Moul78: Mould (1978), Tsuj14: Tsuji & Nakajima (2014), Naka15: Nakajima et al. (2015), Schi97: Schiavon et al. (1997), Gaid14: Gaidos & Mann (2014), Neve14: Neves et al. (2014), Bran21: Brandt et al. (2021).

models, we find a subsolar metallicity which is within 1σ and 2σ of the value reported for Gl 229A in Schiavon et al. (1997) and Neves et al. (2014), respectively. However, our derived metallicity skews subsolar due to retrieved oxygen abundances that are lower than expected for both models. Subsequently, we use carbon as a tracer for overall object metallicity (J. Gaarn et al. 2022, in preparation) and calculate $[C/H] = -0.01 \pm 0.05$ (best fit model) and $[C/H] = 0.05 \pm 0.03$ (mass constrained model). A roughly Solar metallicity is in agreement with all published values for Gl 229A, except Leggett et al. (2002a) which reports a distinctly subsolar metallicity.

We list in Table 6 the retrieval-based C/O ratio for Gl 229B and in Table 7 the C/O ratio reported for Gl 229A from Nakajima et al. (2015). Nakajima et al. (2015) determines a C/O ratio using carbon and oxygen abundances from Tsuji & Nakajima (2014) and Tsuji et al. (2015), a notoriously difficult task for M dwarfs due to molecular absorption features throughout their spectra. Tsuji & Nakajima (2014) and Tsuji et al. (2015) use CO as an indicator of bulk carbon abundance and H₂O as an indicator of bulk oxygen abundance, finding $\log A_C = -3.27 \pm 0.07$ and $\log A_O = -3.10 \pm 0.02$, respectively. The C/O ratio we find in this work is calculated based on the abundances of all retrieved carbon-bearing molecules (CH₄, CO) as compared to all retrieved oxygen-bearing molecules (H₂O, CO). We apply a correction to the oxygen abundance (30% increase) to account for oxygen sequestered in silicate grains deeper in the atmosphere (Line et al. 2015, 2017; Zalesky et al. 2019, 2022). For this correction, we assume the primary oxygen sink is enstatite (Mg₂Si₂O₆) and therefore account for the removal of three oxygen atoms for every magnesium silicate. We do this in an attempt to probe at a bulk, as opposed to atmospheric, C/O ratio for Gl 229B, but note that this correction is still an approximation of the chemistry happening in the interior. The carbon and oxygen abundances of Gl 229A, B are listed in Table 8 for ease of comparison.

It is evident for both best fit and mass constrained models that our C/O ratios are not in agreement with that of the primary. Our best fit retrieved C/O is in agreement within 3σ and our mass constrained, 4σ . Despite the median reported value for Gl 229A being supersolar, our C/O ratios are both >1 . C/O ratio is theorized as a tracer of formation mechanism such that stellar companions with elevated C/O ratios as compared to their primary likely formed due to core accretion in the disk (e.g., Lodders 2004; Madhusudhan et al. 2011;

Table 8
Carbon and Oxygen Abundances

	$\log A_C$	$\log A_O$	C/O Ratio
Gl 229A	-3.27 ± 0.07^a	-3.10 ± 0.02^b	0.68 ± 0.12^c
Gl 229B (BF)	-3.35 ± 0.05	$-3.49^{+0.05}_{-0.04}$	$1.38^{+0.08}_{-0.07}$
Gl 229B (BF) ^d	-3.35 ± 0.05	$-3.38^{+0.05}_{-0.04}$	$1.06^{+0.06}_{-0.05}$
Gl 229B (MC)	-3.29 ± 0.03	-3.45 ± 0.04	1.45 ± 0.07
Gl 229B (MC) ^d	-3.29 ± 0.03	-3.34 ± 0.04	$1.11^{+0.06}_{-0.05}$

Notes. (BF) indicates results from the best fit retrieval model while (MC) indicates results from the best fit model with a mass constraint.

^a Tsuji & Nakajima (2014).

^b Tsuji et al. (2015).

^c Nakajima et al. (2015).

^d Corrected oxygen abundance and subsequent C/O ratio (see Section 8).

Öberg et al. 2011; Madhusudhan 2012; Konopacky et al. 2013). While we do find higher C/O ratios in our models for Gl 229B, it is extremely unlikely that an object $\geq 50 M_{\text{Jup}}$ formed by core accretion in a disk around an M1V star (Bowler et al. 2015; Schlaufman 2018; Mercer & Stamatellos 2020). Furthermore, we compare the abundances of carbon and oxygen and find that the carbon values for both the best fit and mass constrained model agree with that of the primary within 1.2σ and 1σ , respectively. We find this as evidence of coevality and consider the disagreement in oxygen abundance as a result of unexplained chemistry in the atmosphere of Gl 229B. As in Line et al. (2017), we consider that a better understanding of the thermo-chemical mechanisms producing oxygen-bearing condensates is required to estimate a true oxygen abundance in cooler atmospheres. While magnesium silicates are the dominating oxygen sink in brown dwarf atmospheres, we hypothesize additional oxygen sinks, such as iron silicates, could contribute to an oxygen-depleted atmosphere. However, an origin for such influential abundances of alternative metals is unknown.

To place our work in context with another retrieval analysis on Gl 229B, we turn again to the results from Howe et al. (2022). As a result of the increased abundance of oxygen-bearing absorbers as compared to our best fit model (see Section 7), it is not surprising that they find a relatively smaller C/O ratio of 1.13 ± 0.03 . It is also important to note that this work does not make an oxygen correction as we do, which would likely decrease this ratio even further. However, our

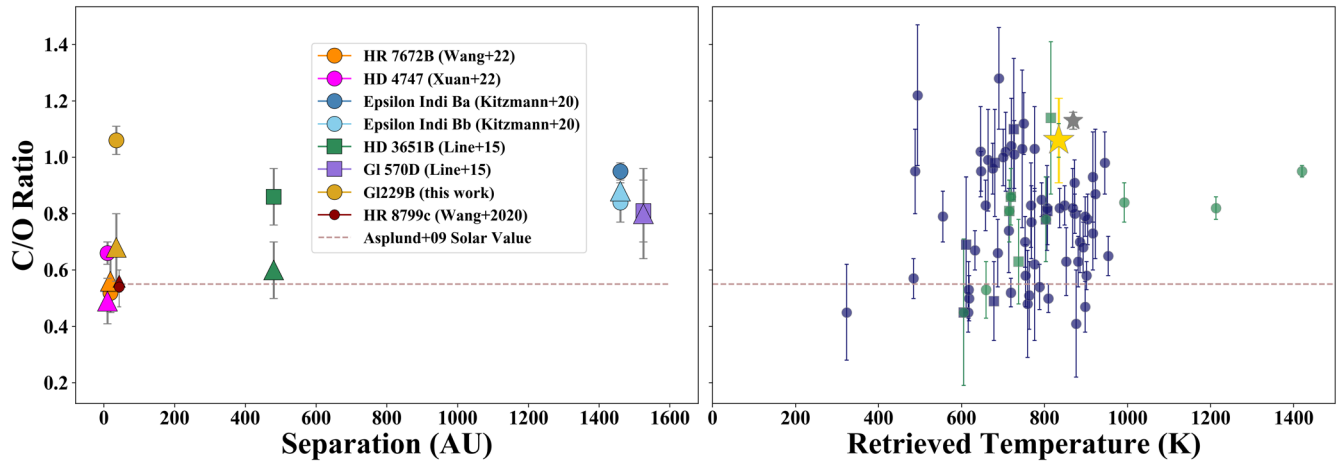


Figure 7. In the figure on the left, we show retrieved C/O values for objects with a main sequence companion with known C/O. Substellar objects are marked by a circle or square while their stellar primaries are marked by a triangle. On the right, we show a sample of brown dwarfs with retrieved C/O taken from Line et al. (2015), Line et al. (2017), Gonzales et al. (2020), Zalesky et al. (2019, 2022), Kitzmann et al. (2020) and Howe et al. (2022). Points in dark blue are isolated objects, while points shown in green are companions. Gl 229B results from this work are marked by a yellow star, whereas Gl 229B results from Howe et al. (2022) are marked by a gray star. Across both plots, objects marked by a circle denote the reported bulk C/O ratio, while squares denote the C/O reported as $\text{CH}_4/\text{H}_2\text{O}$. The dashed line in both plots shows the Solar C/O ratio of 0.55 taken from Asplund et al. (2009).

work does align with Howe et al. (2022) in finding an overall supersolar C/O ratio, which, in their work, was speculated to be a result of unresolved disequilibrium chemistry in the atmosphere of Gl 229B.

8.2. C/O and Metallicity of Gl 229B Compared to Other Retrieved Isolated T Dwarfs

There has been a noticeable trend developing toward supersolar C/O ratios in retrieval models of late T dwarfs, to which our work on Gl 229B now contributes (Figure 7). It is unclear whether this is a nod toward formation pathways, unresolved atmospheric chemistry in these types of objects or a bias in retrieval codes. This is certainly an active area of research that highlights the importance of brown dwarf companions, where studies can be anchored by the chemistry of the primary star (e.g., J. Gaarn et al. 2022, in preparation). In this section, we return to the retrievals of Zalesky et al. (2019, 2022) and Line et al. (2017) to add our work to the growing chemical trends previously reported in these works.

Of the 11 T dwarfs retrieved in Line et al. (2017), seven are isolated brown dwarfs with no potential for comparative chemistry to a Solar-type star. However, whether companion or not, a similar trend emerges for the entire sample of T dwarfs toward supersolar C/O ratio, even after the implemented oxygen correction factor. Of these seven isolated objects, six were reported to have supersolar C/O ratios in the range 0.63–1.14. It is important to make a distinction here that, as a result of unconstrained CO and CO_2 , Line et al. (2017) calculated both C/O ratio and metallicity using CH_4 and H_2O abundances only. We note this because non-equilibrium chemistry, particularly with CO, could be a factor in the oxygen depletion seen in these retrievals. As a result, unconstrained abundances for CO and CO_2 could possibly be driving supersolar C/O ratios rather than unresolved chemistry or code biases.

Next, we consider our work against Zalesky et al. (2019, 2022) which initially presented retrieval models of a sample of 14 isolated late-type T dwarfs and Y dwarfs (T8–Y1), later expanded to a sample of 50 late-type T dwarfs (T7–T9). Of the six T dwarfs in the Zalesky et al. (2019) sample (T8–T9.5), they again find a trend toward supersolar C/O ratio in the late T regime with

derived values in the range 0.7–1.47 (with exception for one T9 object with a retrieved C/O of 0.57 ± 0.07). In this work, the C/O ratio is calculated using H_2O , CH_4 , CO and CO_2 , despite only having upper limits on CO and CO_2 . Consistent with Line et al. (2017), Zalesky et al. (2019) also includes a C/O correction factor of 30%. Unlike our work, Zalesky et al. (2019) reports slightly enhanced metallicities for this subset of T dwarfs. However, they report no apparent trend between high C/O and metallicity for late-T objects. Building on this initial study, Zalesky et al. (2022) also reports supersolar C/O ratios in range 0.65–1.28 for approximately 75% of their sample. For the comparative objects we discussed in 7, WISEJ024124.73 – 365328.0 has a retrieved C/O ratio of 0.82 ± 0.07 , WISEJ112438.12 – 042149.7 a value of $0.83^{+0.07}_{-0.08}$, and WISEPCJ221354.69 + 091139.4, $0.63^{+0.12}_{-0.08}$. As our chemical abundances for Gl 229B were most similar to WISEJ024124.73 – 365328.0 and WISEJ112438.12 – 042149.7, it is not surprising that we find our C/O ratio closer in value to these objects than WISEPCJ221354.69 + 091139.4. While our model for Gl 229B still reports a higher C/O ratio than all three of these temperature comparisons, we can still place our model alongside this apparent trend of supersolar C/O ratios in T dwarf retrievals. We visualize this trend in 7.

8.3. C/O and Metallicity of Gl 229B Compared to Other Companion Objects

The appeal of studying companion objects lies largely in the draw of understanding formation pathways. For brown dwarfs specifically, we hope that by comparing the atmospheric chemistry to that of its primary star (or brown dwarf companion) we can probe at the system age and make a determination as to whether the two objects formed together and if they formed in the same way (i.e., via gravitational fragmentation). As brown dwarf formation mechanisms are still unclear, studying co-moving systems provides one possible path to make advances in this topic.

In this section, we compare our findings on the Gl 229 system to the comparative chemistry of co-moving systems Gl 570 and HD 3651 (Line et al. 2015, 2017), ϵ Indi (Kitzmann et al. 2020), HR 8799 (Konopacky et al. 2013; Ruffio et al. 2021) and HR 7672 (Wang et al. 2022). We also plot the C/O ratios of these

brown dwarf companion systems in Figure 7. These systems are of particular interest in relation to this work since they are all subjects of retrieval studies. Since Gl 570D, HD 3651B and ϵ Indi Bb are all late-T type objects, we would expect similar trends to emerge chemically (i.e., a high C/O ratio due to sequestered oxygen). However, we use the HR 8799 and HR 7672 systems as potential contrast, as we would not necessarily expect the same thermodynamic behavior in objects significantly hotter or cooler than Gl 229B. By placing the Gl 229 system in context with other retrieved co-moving systems, we can investigate trends in chemical abundance across companion objects with the ultimate goal of understanding underlying brown dwarf chemistry and formation.

Gl 570 (K4V+T7.5): Gl 570D is an ideal companion candidate, as it is widely separated from a well-studied main sequence star, Gl 570A. Line et al. (2015) reports metallicity and C/O ratio for the primary as 0.05 ± 0.17 and 0.81 ± 0.16 , respectively. As previously discussed, Line et al. (2015, 2017) applies a correction to the retrieved atmospheric oxygen abundance to probe at bulk abundance for Gl 570D, giving metallicity and C/O ratio values of $-0.15^{+0.07}_{-0.09}$ and $0.79^{+0.28}_{-0.23}$, respectively. While the spread for C/O spans the range of solar to supersolar and metallicity spans subsolar to solar, there is agreement to 1σ for these chemical parameters between Gl 570D and its primary, which is in contrast to our model.

HD 3651 (K0V+T7.5): HD 3651B is another widely separated companion to a well-studied main sequence star, HD 3651A. Line et al. (2015) reports metallicity and C/O ratio for the primary as 0.18 ± 0.07 and 0.62 ± 0.11 , respectively. The oxygen-corrected metallicity and C/O ratio of HD 3651B are $0.08^{+0.05}_{-0.06}$ and $0.89^{+0.21}_{-0.17}$, respectively. Clearly, this system shares a similarity to our work in that the primary star is of solar C/O and its brown dwarf companion is distinctly supersolar.

ϵ Indi (K4.5V + T1.5 + T6.5): The ϵ Indi system is another useful example where the main sequence primary can help put constraints on fundamental parameters. King et al. (2010) reports a metallicity measurement of -0.2 for the primary which is in agreement only with ϵ Indi Bb, the T6.5 dwarf, at a retrieved value of $-0.34^{+0.12}_{-0.11}$. The subsolar metallicity is predicted by the chemistry of the primary star. However, this work does not correct for condensation of oxygen-bearing condensates, so we would expect better agreement after this assumption. A supersolar C/O ratio reported for both ϵ Indi Bb at 0.84 ± 0.07 and ϵ Indi Ba at 0.95 ± 0.03 is also predicted to be closer to solar after a correction. Similar to Line et al. (2015, 2017) this work was not able to place constraints on CO, CO₂, or H₂S, but does, in fact, calculate a C/O with all oxygen- and carbon-bearing molecules. Another interesting feature of this work, similar to ours, is that dynamical measurements predicted both brown dwarf companions to be $\sim 50 - 70 M_{\text{Jup}}$ (Dieterich et al. 2018; Chen et al. 2022), while retrieval models place Ba and Bb at $50^{+7.8}_{-6.6}$ and $15^{+6}_{-4.6} M_{\text{Jup}}$, respectively.

HD 7672 (G0+L4): HD 7672 is another system in which the solar-type primary is well studied, with reported abundances [Fe/H] = -0.04 ± 0.07 , [C/H] = -0.08 ± 0.05 , [O/H] = 0.15 ± 0.06 and C/O = 0.56 ± 0.11 (Wang et al. 2022). Retrieval-derived abundance for the brown dwarf companion are reported as [C/H] = -0.24 ± 0.05 , [O/H] = -0.19 ± 0.06 and C/O = 0.52 ± 0.02 . This is an interesting divergence from our work where the C/O ratio is within 1σ agreement to its primary, but [C/H], which we use as a proxy for overall object metallicity,

is subsolar. Since this brown dwarf companion is an L-type, we should not need to correct for oxygen-bearing condensates, although Wang et al. (2022) does state that retrieved carbon and oxygen abundances are atmospheric (as opposed to bulk) and suggests that inefficient mixing could be a cause of these metallicity differences.

HR 8799 (A5/F0+bcde): This system provides an interesting contrast to ours, as this young star has four substellar companions with masses in the range 5–13 M_{Jup} orbiting within 15–70 AU, which is beyond the H₂O ice line in the disk (Konopacky et al. 2013). Initial studies from Konopacky et al. (2013), found enhanced C/O ratio for the b, c companions as compared to the primary, which is approximately solar at $0.54^{+0.12}_{-0.09}$, suggesting a core accretion scenario. However, Ruffio et al. (2021) concluded that all four planets have stellar C/O ratios, which could imply either core accretion or gravitational instability as a formation mechanism. This result is in agreement with retrieval results on HR 8799c,e (Mollière et al. 2020; Wang et al. 2020) but in disagreement with the retrieval study of Lavie et al. (2017), which found all four companions to be oxygen-enriched relative to their star. This opens up a particularly interesting discussion on the usefulness of the C/O ratio as a formation diagnostic for objects near or above the deuterium burning limit. We include HR 8799c in Figure 7 as a contrast to higher mass, brown dwarf companions that show distinct supersolar C/O trends, as well as chemical non-uniformity to their primary star.

While the C/O ratio has the potential to be a powerful formation diagnostic, the complications that arise in our attempt to determine bulk C/O ratios in substellar objects currently prevent us from using it as conclusive evidence. While we expect oxygen depletion in T-type objects, we still see unexpectedly incongruous C/O ratios for the Gl 229, HD 3651 and ϵ Indi systems. However, retrieval studies on Gl 570 and HD 7672 were able to match C/O ratio across companions within 1σ . Additionally, in the HR 8799 system where we initially predicted superstellar C/O ratios, retrieval results found substellar or stellar ratios. From these varied retrieval results so far, we do not see a unique chemical trend emerging (i.e., anomalously high C/O ratios for all T-type objects, indicating unresolved chemistry in that temperature regime or anomalously high C/O ratios for all brown dwarfs, suggesting a retrieval code bias). However, we also consider the possibility that both unresolved chemistry and code bias are contributing to the retrieval results we present.

9. Conclusions

In this work we present an updated distance-calibrated SED and retrieval model of Gl 229B. Gl 229B is best fit by a cloudless model, which is in agreement with previous retrieval work on T dwarfs (Line et al. 2015, 2017; Gonzales et al. 2020; Zalesky et al. 2022), as well as prior forward model predictions (i.e., Allard et al. 1996; Saumon et al. 2000; Leggett et al. 2002a). We find that our retrieved mass and log(g) are consistent with evolutionary model predictions to within 1σ . However, we do find that our T_{eff} is slightly cooler than its SED-derived value, which is a result of the retrieved radius being larger than predicted. We also find the use of Allard alkalis provides a better spectral fit than Burrows, consistent with Gonzales et al. (2020).

Additionally, we find that a cloud-free model, with a prior constraint on mass near its dynamical value from Brandt et al.

(2021), is capable of reproducing the chemistry and fit to the observed spectrum consistently well as our best fit cloud-free model. Although we make no age determination, we find it plausible that Gl 229B is a $70 M_{\text{Jup}}$ object.

We discuss the implications of an anomalously high C/O ratio, especially as compared to its stellar value. We make a 30% correction for oxygen sequestered into condensates deep below the photosphere and still find a C/O ratio > 1 for our best fit model. We find this work contributes to a trend in brown dwarf retrievals toward supersolar C/O ratios, particularly for T dwarfs. We also note that this high C/O ratio is due solely to “missing” oxygen in the atmosphere, as we can match the abundance of carbon to its reported stellar value. As a result, we use [C/H] as a marker for overall metallicity and find that Gl 229B is of solar metallicity, as the literature predicts. While we cannot unify the dissimilarity in C/O between Gl 229B and its primary, we find the agreement in carbon abundance a strong nod toward co-evity. Overall, these results lead us toward more questions on the nature of brown dwarf atmospheric chemistry, formation, evolution and even biases in modeling approaches that we plan to explore in future work.

The data used in this publication were collected through the MENDEL high performance computing (HPC) cluster at the American Museum of Natural History. This HPC cluster was developed with National Science Foundation (NSF) Campus Cyberinfrastructure support through Award 1925590. This

work was also supported by the National Science Foundation via awards 1909776, 1614527 and AST-1909837.

Software: astropy (Astropy Collaboration et al. 2013), Brewster (Birmingham et al. 2017), Corner (Foreman-Mackey 2016), EMCEE (Foreman-Mackey et al. 2013), PyMultinest (Buchner 2014), SEDkit (Filippazzo et al. 2015).

Appendix Comments on Alkalies Used in Retrieval

The use of Allard opacities for T dwarf retrievals follows the work of Gonzales et al. (2020) that found that Burrows opacities produced retrieved alkali abundances that were incongruous with expected values due to rainout in T dwarfs. We also find the use of Allard opacities is strongly preferred by our model, as determined by the Bayesian selection criterion, where a cloudless model with Burrows opacities is strongly rejected as compared to our best fit model (Table 4). We confirm these results by the spectral fit of a cloudless model with Burrows opacities, see Figure A1. It is clear that there is an extremely poor fit of the K-I feature in the *J*-band where the model predicted a much stronger absorption line than exists in the observed data. As discussed in Section 5.1, we find that a cloudless model using Allard opacities can, in fact, fit this alkali feature.

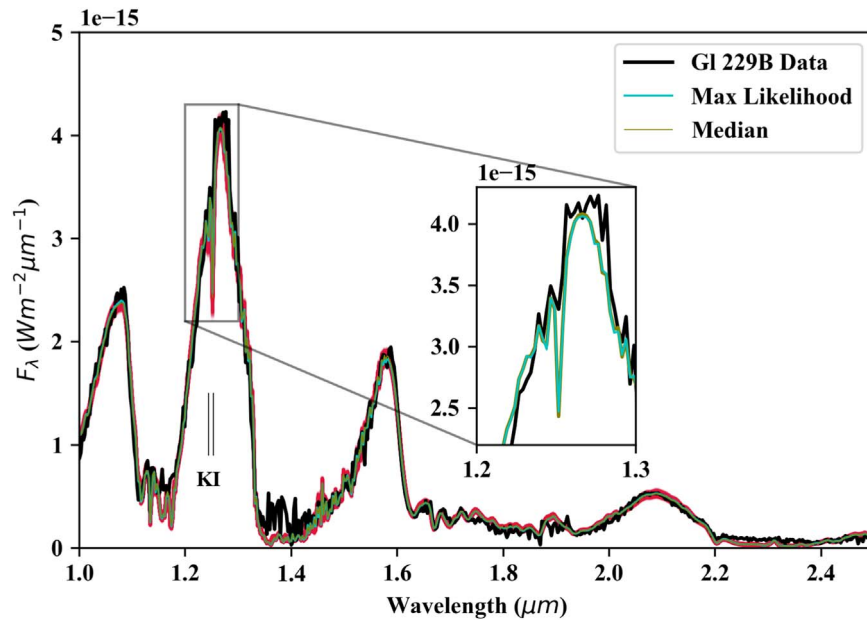










Figure A1. This figure shows the results of a cloudless model with Burrows alkalies where the spectral fit to the K-I doublet in the *J* spectral band (around $1.25 \mu\text{m}$) is severely overestimated. Observed data is shown in black, whereas the maximum likelihood retrieved spectrum is in blue. This model used a wavelength coverage of $1.0\text{--}5.0 \mu\text{m}$, however, we shorten the wavelength coverage in this figure to give a clearer view of this alkali feature. This serves as a comparison to our best fit model which uses Allard alkalies and shows an objectively good fit in this region.

ORCID iDs

Emily Calamari  <https://orcid.org/0000-0002-2682-0790>
 Jacqueline K. Faherty  <https://orcid.org/0000-0001-6251-0573>
 Ben Burningham  <https://orcid.org/0000-0003-4600-5627>
 Eileen Gonzales  <https://orcid.org/0000-0003-4636-6676>
 Daniella Bardalez-Gagliuffi  <https://orcid.org/0000-0001-8170-7072>
 Johanna M. Vos  <https://orcid.org/0000-0003-0489-1528>
 Marina Gemma  <https://orcid.org/0000-0002-8871-773X>
 Niall Whiteford  <https://orcid.org/0000-0001-8818-1544>

References

- Allard, F., Allard, N. F., Homeier, D., et al. 2007a, *A&A*, 474, L21
 Allard, F., Hauschildt, P. H., Alexander, D. R., Tamanai, A., & Schweitzer, A. 2001, *ApJ*, 556, 357
 Allard, F., Hauschildt, P. H., Baraffe, I., & Chabrier, G. 1996, *ApJL*, 465, L123
 Allard, N. F., Spiegelman, F., & Kielkopf, J. F. 2007b, *A&A*, 465, 1085
 Angus, R., Morton, T. D., Foreman-Mackey, D., et al. 2019, *AJ*, 158, 173
 Asplund, M., Grevesse, N., Sauval, A. J., & Scott, P. 2009, *ARA&A*, 47, 481
 Astropy Collaboration, Robitaille, T. P., Tollerud, E. J., et al. 2013, *A&A*, 558, A33
 Baraffe, I., Chabrier, G., Allard, F., & Hauschildt, P. H. 2002, *A&A*, 382, 563
 Baraffe, I., Chabrier, G., Barman, T. S., Allard, F., & Hauschildt, P. H. 2003, *A&A*, 402, 701
 Bowler, B. P., Liu, M. C., Shkolnik, E. L., & Tamura, M. 2015, *ApJS*, 216, 7
 Brandt, G. M., Dupuy, T. J., Li, Y., et al. 2021, *AJ*, 162, 301
 Brandt, T. D., Dupuy, T. J., Bowler, B. P., et al. 2020, *AJ*, 160, 196
 Buchner, J. 2014, *S&C*, 26, 383
 Burgasser, A. J., Cruz, K. L., & Kirkpatrick, J. D. 2007, *ApJ*, 657, 494
 Burgasser, A. J., Geballe, T. R., Leggett, S. K., Kirkpatrick, J. D., & Golimowski, D. A. 2006, *ApJ*, 637, 1067
 Burningham, B., Marley, M. S., Line, M. R., et al. 2017, *MNRAS*, 470, 1177
 Burningham, B., Pinfield, D. J., Leggett, S. K., et al. 2009, *MNRAS*, 395, 1237
 Burningham, B., Leggett, S. K., Homeier, D., et al. 2011, *MNRAS*, 414, 3590
 Burningham, B., Cardoso, C. V., Smith, L., et al. 2013, *MNRAS*, 433, 457
 Burningham, B., Faherty, J. K., Gonzales, E. C., et al. 2021, *MNRAS*, 506, 1944
 Burrows, A., Hubbard, W. B., Saumon, D., & Lunine, J. I. 1993, *ApJ*, 406, 158
 Burrows, A., Marley, M. S., & Sharp, C. M. 2000, *ApJ*, 531, 438
 Burrows, A., & Volobuyev, M. 2003, *ApJ*, 583, 985
 Burrows, A., Marley, M., Hubbard, W. B., et al. 1997, *ApJ*, 491, 856
 Chabrier, G., & Baraffe, I. 1997, *A&A*, 327, 1039
 Chabrier, G., Baraffe, I., Allard, F., & Hauschildt, P. 2000, *ApJ*, 542, 464
 Chen, M., Li, Y., Brandt, T. D., et al. 2022, *AJ*, 163, 288
 Cushing, M. C., Roellig, T. L., Marley, M. S., et al. 2006, *ApJ*, 648, 614
 Cushing, M. C., Marley, M. S., Saumon, D., et al. 2008, *ApJ*, 678, 1372
 Cushing, M. C., Kirkpatrick, J. D., Gelino, C. R., et al. 2011, *ApJ*, 743, 50
 Dieterich, S. B., Weinberger, A. J., Boss, A. P., et al. 2018, *ApJ*, 865, 28
 Dupuy, T. J., Liu, M. C., & Ireland, M. J. 2009, *ApJ*, 692, 729
 Faherty, J. K., Burgasser, A. J., West, A. A., et al. 2010, *AJ*, 139, 176
 Faherty, J. K., Goodman, S., Caselden, D., et al. 2020, *ApJ*, 889, 176
 Faherty, J. K., Gagne, J., Popinchalk, M., et al. 2021, *ApJ*, 923, 48
 Fegley, B. J., & Lodders, K. 1994, *Icar*, 110, 117
 Fegley, B. J., & Lodders, K. 1996, *ApJL*, 472, L37
 Feroz, F., Hobson, M. P., & Bridges, M. 2009, *MNRAS*, 398, 1601
 Filippazzo, J. C., Rice, E. L., Faherty, J., et al. 2015, *ApJ*, 810, 158
 Foreman-Mackey, D. 2016, *JOSS*, 1, 24
 Foreman-Mackey, D., Hogg, D. W., Lang, D., & Goodman, J. 2013, *PASP*, 125, 306
 Freedman, R. S., Lustig-Yaeger, J., Fortney, J. J., et al. 2014, *ApJS*, 214, 25
 Freedman, R. S., Marley, M. S., & Lodders, K. 2008, *ApJS*, 174, 504
 Gaia Collaboration, Klioner, S. A., Migard, F., et al. 2021, *A&A*, 649, A9
 Gaidos, E., & Mann, A. W. 2014, *ApJ*, 791, 54
 Gao, P., Thorngren, D. P., Lee, E. K. H., et al. 2020, *NatAs*, 4, 951
 Geballe, T. R., Kulkarni, S. R., Woodward, C. E., & Sloan, G. C. 1996, *ApJL*, 467, L101
 Golimowski, D. A., Burrows, C. J., Kulkarni, S. R., Oppenheimer, B. R., & Brukardt, R. A. 1998, *AJ*, 115, 2579
 Golimowski, D. A., Leggett, S. K., Marley, M. S., et al. 2004, *AJ*, 127, 3516
 Gonzales, E. C., Burningham, B., Faherty, J. K., et al. 2020, *ApJ*, 905, 46
 Gonzales, E. C., Burningham, B., Faherty, J. K., et al. 2021, *ApJ*, 923, 19
 Hansen, J. E. 1971, *JATIS*, 28, 1400
 Helling, C., & Casewell, S. 2014, *A&ARv*, 22, 80
 Hewett, P. C., Warren, S. J., Leggett, S. K., & Hodgkin, S. T. 2006, *MNRAS*, 367, 454
 Holstein, T. 1950, *PhRv*, 79, 744
 Holtsmark, J. 1925, *ZPhy*, 34, 722
 Howe, A. R., Burrows, A., & Deming, D. 2017, *ApJ*, 835, 96
 Howe, A. R., McElwain, M. W., & Mandell, A. M. 2022, *ApJ*, 935, 107
 Kass, R. E., & Raftery, A. E. 1995, *JASA*, 90, 773
 King, R. R., McCaughrean, M. J., Homeier, D., et al. 2010, *A&A*, 510, A99
 Kirkpatrick, J. D. 2005, *ARA&A*, 43, 195
 Kirkpatrick, J. D., Dahn, C. C., Monet, D. G., et al. 2001, *AJ*, 121, 3235
 Kirkpatrick, J. D., Henry, T. J., & McCarthy, D. W., Jr. 1991, *ApJS*, 77, 417
 Kitzmann, D., Heng, K., Oreshenko, M., et al. 2020, *ApJ*, 890, 174
 Konopacky, Q. M., Barman, T. S., Macintosh, B. A., & Marois, C. 2013, *Sci*, 339, 1398
 Lavie, B., Mendonça, J. M., Mordasini, C., et al. 2017, *AJ*, 154, 91
 Leggett, S. K. 1992, *ApJS*, 82, 351
 Leggett, S. K., Hauschildt, P. H., Allard, F., Geballe, T. R., & Baron, E. 2002a, *MNRAS*, 332, 78
 Leggett, S. K., Toomey, D. W., Geballe, T. R., & Brown, R. H. 1999, *ApJL*, 517, L139
 Leggett, S. K., Golimowski, D. A., Fan, X., et al. 2002b, *ApJ*, 564, 452
 Liebert, J., Reid, I. N., Burrows, A., et al. 2000, *ApJL*, 533, L155
 Line, M. R., Teske, J., Burningham, B., Fortney, J. J., & Marley, M. S. 2015, *ApJ*, 807, 183
 Line, M. R., Marley, M. S., Liu, M. C., et al. 2017, *ApJ*, 848, 83
 Lodders, K. 1999, *ApJ*, 519, 793
 Lodders, K. 2002, *ApJ*, 577, 974
 Lodders, K. 2004, *ApJ*, 611, 587
 Lodders, K. 2010, *ApSSP*, 16, 379
 Lodders, K., & Fegley, B. 2002, *Icar*, 155, 393
 Lodders, K., & Fegley, B. 2006, in *Astrophysics Update 2*, ed. J. W. Mason (Chichester: Springer Praxis Books), 1
 Madhusudhan, N. 2012, *ApJ*, 758, 36
 Madhusudhan, N., Mousis, O., Johnson, T. V., & Lunine, J. I. 2011, *ApJ*, 743, 191
 Manjavacas, E., Bonnefoy, M., Schlieder, J. E., et al. 2014, *A&A*, 564, A55
 Marley, M. S. 1997, arXiv:astro-ph/9706234
 Marley, M. S., Ackerman, A. S., Cuzzi, J. N., & Kitzmann, D. 2013, in *Comparative Climatology of Terrestrial Planets*, ed. S. J. Mackwell, M. Bullock, J. Harder et al. (Tucson, AZ: Univ. Arizona Press), 367
 Marley, M. S., & Robinson, T. D. 2015, *ARA&A*, 53, 279
 Marley, M. S., Saumon, D., Guillot, T., et al. 1996, *Sci*, 272, 1919
 Marley, M. S., Seager, S., Saumon, D., et al. 2002, *ApJ*, 568, 335
 Marley, M. S., Saumon, D., Visscher, C., et al. 2021, *ApJ*, 920, 85
 Matthews, K., Nakajima, T., Kulkarni, S. R., & Oppenheimer, B. R. 1996, *AJ*, 112, 1678
 McBride, B. J., & Gordon, S. D. 1994, Computer Program for Calculation of Complex Chemical Equilibrium Compositions and Applications I. Analysis, Reference Publication NASA RP-1311, NASA Lewis Research Center
 McKay, C. P., Pollack, J. B., Zent, A. P., Cruikshank, D. P., & Courtin, R. 1989, *GeoRL*, 16, 973
 Mercer, A., & Stamatellos, D. 2020, *A&A*, 633, A116
 Mollière, P., Stolker, T., Lacour, S., et al. 2020, *A&A*, 640, A131
 Morley, C. V., Fortney, J. J., Marley, M. S., et al. 2012, *ApJ*, 756, 172
 Moses, J. I., Richardson, M. R., Madhusudhan, N., et al. 2012, AAS/Division for Planetary Sciences Meeting Abstracts, 44, 103.02
 Moses, J. I., Line, M. R., Visscher, C., et al. 2013, *ApJ*, 777, 34
 Mould, J. R. 1978, *ApJ*, 226, 923
 Nakajima, T., Oppenheimer, B. R., Kulkarni, S. R., et al. 1995, *Natur*, 378, 463
 Nakajima, T., Tsuji, T., & Takeda, Y. 2015, *AJ*, 150, 53
 Neves, V., Bonfils, X., Santos, N. C., et al. 2014, *A&A*, 568, A121
 Noll, K. S., Geballe, T. R., & Marley, M. S. 1997, *ApJL*, 489, L87
 Öberg, K. I., Murray-Clay, R., & Bergin, E. A. 2011, *ApJL*, 743, L16
 Oppenheimer, B. R., Kulkarni, S. R., Matthews, K., & Nakajima, T. 1995, *Sci*, 270, 1478
 Oppenheimer, B. R., Kulkarni, S. R., Matthews, K., & van Kerkwijk, M. H. 1998, *ApJ*, 502, 932
 Perryman, M. A. C., Lindegren, L., Kovalevsky, J., et al. 1997, *A&A*, 323, L49
 Phillips, M. W., Tremblin, P., Baraffe, I., et al. 2020, *A&A*, 637, A38
 Pinfield, D. J., Burningham, B., Lodieu, N., et al. 2012, *MNRAS*, 422, 1922
 Rice, E. L., Barman, T., Mclean, I. S., Prato, L., & Kirkpatrick, J. D. 2010, *ApJS*, 186, 63
 Ruffio, J.-B., Konopacky, Q. M., Barman, T., et al. 2021, *AJ*, 162, 290
 Saumon, D., Geballe, T. R., Leggett, S. K., et al. 2000, *ApJ*, 541, 374
 Saumon, D., & Marley, M. S. 2008, *ApJ*, 689, 1327
 Schiavon, R. P., Barbuy, B., & Singh, P. D. 1997, *ApJ*, 484, 499
 Schlaufman, K. C. 2018, *ApJ*, 853, 37

- Schultz, A. B., Allard, F., Clampin, M., et al. 1998, [ApJL](#), 492, L181
- Toon, O. B., McKay, C. P., Ackerman, T. P., & Santhanam, K. 1989, [JGR](#), 94, 16287
- Tsuji, T., & Nakajima, T. 2014, [PASJ](#), 66, 98
- Tsuji, T., Nakajima, T., & Takeda, Y. 2015, [PASJ](#), 67, 26
- Visscher, C. 2012, [ApJ](#), 757, 5
- Visscher, C., Lodders, K., & Fegley, B. J. 2006, [ApJ](#), 648, 1181
- Visscher, C., Lodders, K., & Fegley, B. J. 2010, [ApJ](#), 716, 1060
- Visscher, C., & Moses, J. I. 2011, [ApJ](#), 738, 72
- Wakeford, H. R., & Sing, D. K. 2015, [A&A](#), 573, A122
- Wang, J., Wang, J. J., Ma, B., et al. 2020, [AJ](#), 160, 150
- Wang, J., Kolecki, J. R., Ruffio, J.-B., et al. 2022, [ApJ](#), 163, 189
- West, A. A., Hawley, S. L., Bochanski, J. J., et al. 2008, [AJ](#), 135, 785
- Zahnle, K. J., & Marley, M. S. 2014, [ApJ](#), 797, 41
- Zalesky, J. A., Line, M. R., Schneider, A. C., & Patience, J. 2019, [ApJ](#), 877, 24
- Zalesky, J. A., Saboi, K., Line, M. R., et al. 2022, [ApJ](#), 936, 44